Red blood cell tension protects against severe malaria in the Dantu blood group

Silvia N. Kariuki[1*], Alejandro Marin-Menendez[2*], Viola Introini[3*], Benjamin J. Ravenhill[4], Yen-Chun Lin[3], Alex Macharia[1], Johnstone Makale[1], Metrine Tendwa[1], Wilfred Nyamu[1], Jurij Kotar[3], Manuela Carrasquilla[2], J. Alexandra Rowe[5], Kirk Rockett[6], Dominic Kwiatkowski[2,6,7], Michael P. Weekes[4], Pietro Cicuta[3$#], Thomas N. Williams[1,8$#], Julian C. Rayner[2,4$#]

[1]KEMRI-Wellcome Trust Research Programme, Kilifi, Kenya

[2]Wellcome Sanger Institute, Cambridge, UK

[3]Cavendish Laboratory, University of Cambridge, Cambridge, UK

[4]Cambridge Institute for Medical Research, University of Cambridge, Cambridge, UK

[5]University of Edinburgh, Edinburgh, UK

[6]Wellcome Centre for Human Genetics, University of Oxford, Oxford, UK

[7]Big Data Institute, University of Oxford, Oxford, UK

[8]Imperial College London, London, UK

* equal contributions

$ jointly supervising

corresponding

Pietro Cicuta, Cavendish Laboratory, University of Cambridge, Cambridge CB3 0HE, United Kingdom. Phone: +44 1223 337462. E-mail: pc245@cam.ac.uk

Thomas N. Williams, KEMRI-Wellcome Trust Research Programme, Centre for Geographic Medicine Research-Coast, Kilifi 80108, Kenya. E-mail: twilliams@kemri-wellcome.org

Julian C. Rayner, Cambridge Institute for Medical Research, University of Cambridge,

Cambridge CB2 0XY, United Kingdom. Phone: +44 1223 492327. E-mail: jcr1003@cam.ac.uk

Malaria has had a major effect on the human genome, many protective polymorphisms such as sickle cell trait having been selected to high frequencies in malaria endemic regions[1,2]. Recently, it was shown that the blood group variant Dantu provides 74% protection against all forms of severe malaria in homozygous individuals[3-5]. This is a similar degree of protection to sickle cell trait and considerably greater than the best malaria vaccine, but until now the protective mechanism has been unknown. Here, we demonstrate a significant impact of Dantu on *Plasmodium falciparum*-merozoite RBC invasion. Dantu was associated with extensive changes to the RBC surface protein repertoire, but unexpectedly, inhibition did not correlate with specific RBC-parasite receptor-ligand interactions. By following invasion using video microscopy, we found a strong link between RBC tension and merozoite invasion and identified a tension threshold above which invasion rarely occurred, even in non-Dantu RBCs. Dantu RBCs had higher average tension, meaning that a greater proportion resisted invasion. These findings provide both an explanation for the malaria-protective effect of Dantu, and fresh insights into why the efficiency of *P. falciparum* invasion might vary across the heterogenous populations of RBCs both within and between individuals.

The Dantu polymorphism has been fine-mapped to a structural rearrangement in the glycophorin (*GYP*) gene cluster. This rearrangement of the *GYPA* and *GYPB* genes creates two copies of a hybrid gene that encodes the Dantu blood group antigen, a novel sialoglycoprotein composed of a glycophorin B (GYPB) extracellular domain fused with a glycophorin A (GYPA) intracellular domain[5]. Both GYPA and GYPB play important functional roles in the invasion of *P. falciparum* merozoites into RBCs, being receptors for the *P. falciparum* erythrocyte-binding ligand *Pf*EBA-175[6] and the *P. falciparum* erythrocyte binding ligand 1 (*Pf*EBL-1)[7] respectively.

Dantu limits red blood cell invasion

To investigate the impact of Dantu on *P. falciparum* invasion, we collected RBC samples from 42 healthy children from Kilifi in Kenya. Whilst the prevalence of Dantu is limited geographically, being found at much lower frequencies across Africa than the sickle mutation in *HBB* (β^S), it is found at a minor allele frequency (MAF) of approximately 10% in this region, the highest yet described[1,3] and higher than that of β^S in this same area (MAF ~8%[4]). To eliminate any possible confounding from other large-effect malaria-protective polymorphisms, we excluded samples from subjects with either β^S or homozygous α-thalassaemia (**Supplementary Table 1**). We quantified invasion over one life cycle (**Extended Data Fig. 1a**) using a flow-cytometry-based preference assay[8]. Parasites were co-cultured with differentially labelled Dantu-heterozygous, homozygous, and non-Dantu RBCs, and we measured invasion events into each using a fluorescent DNA dye (**Supplementary Figure**). Significantly lower invasion of Dantu RBCs was seen for 3 parasite strains (3D7, Dd2 and SAO75), while a similar but non-significant trend was observed for GB4 and 7G8, potentially because of technical variation in their growth rates and starting parasitaemias. We chose these five strains for their use of varying invasion pathways and their differing reliance on GYPA in particular; Dantu limited invasion in all cases. We also observed a trend towards greater invasion-resistance by Dantu homozygous than heterozygous RBCs, suggesting a dose-dependent effect (**Fig. 1a, Supplementary Table 2**).

To investigate the specific step at which invasion was impaired, we used time-lapse video microscopy to study the invasion process by 3D7 strain parasites. Invasion into Dantu RBCs was also significantly decreased in this real-time assay, independently validating the results of our FACS-based assays (**Fig. 1b and Supplementary Videos 1 and 2**). Invasion can be broken

down into three phases: pre-invasion, invasion and echinocytosis (**Extended Data Fig. 1b**). Even when successful, the early pre-invasion and subsequent entry steps took significantly longer in Dantu homozygous RBCs, suggesting a mechanical resistance to invasion. By contrast, we found no significant difference in the strength of attachment between merozoites and Dantu RBCs using optical tweezers[9] (**Extended Data Fig. 2a, Supplementary Table 3, and Supplementary Video 3**), nor was there a significant difference in the degree of membrane deformation[10] or echinocytosis triggered by parasites invading RBCs of differing Dantu genotype (**Extended Data Fig. 2b and c**). Overall, these results indicate that Dantu has a pleiotropic effect on invasion across both contact and entry phases.

Surface protein composition also affected

Comparing RBC indices across the Dantu genotypic groups revealed significantly lower mean cell volumes (MCVs) and mean cell haemoglobin concentrations in Dantu homozygotes (**Table 1**). This suggests that Dantu directly impacts RBC properties, perhaps by altering the composition of the RBC surface. Despite the fact that Dantu leaves an intact copy of *GYPA* within the genome[5], the surface expression level of GYPA in Dantu RBCs was significantly reduced when measured by flow cytometry (**Fig. 2a**), confirming observations from previous studies[11]. By contrast, surface expression of GYPB was unchanged, while both GYPC, another important invasion receptor[12], and Band 3 were significantly increased in Dantu RBCs (**Fig. 2a**). CR1 levels were lower in heterozygotes compared to the other two genotypes and, importantly, we also observed a significantly higher proportion of Dantu cells expressing CD71, a marker of younger RBCs that is lost with maturation (**Fig. 2a**). The conclusion that Dantu RBCs might be younger is supported by the higher reticulocyte counts (**Table 1**), and a higher reticulocyte RNA content (**Extended Data Fig. 3**) in Dantu homozygotes. We saw no

differences in the surface expression of other essential RBC membrane proteins including Basigin, CD55, CD44, Integrin and Duffy (**Fig. 2a**).

To quantify these changes more accurately, we employed plasma membrane profiling[13] and tandem mass tag mass spectrometry to accurately quantify surface proteins. Analyzing RBCs from three donors of each type revealed widespread cell surface changes, with 40 proteins up- and 34 down-regulated by >50% in Dantu heterozygotes, and 66 proteins up- and 34 down-regulated by >50% in Dantu homozygotes (**Figures 2b, Extended Data Fig. 4, Supplementary Table 4**). The significant decrease in GYPA expression identified by flow cytometry was confirmed by mass spectrometry (**Extended Data Fig. 4b**), which also identified a significant increase in CD71 expression in Dantu homozygotes (**Fig. 2b**), supporting the conclusion that on average, Dantu RBCs are younger than normal RBCs. By contrast, the significant increase in GYPC and Band 3 expression in Dantu RBCs observed by flow cytometry were not confirmed by mass spectrometry. Given the more quantitative nature of mass spectrometry, these are likely the more definitive findings. Mass spectrometry also distinguished peptides unique to GYPA (which were all in the extracellular region of the protein) from those shared with Dantu (which were all intracellular), confirming the presence of Dantu antigen on the RBC surface (**Figure 2c, Extended Data Fig. 4**).

Two independent methods therefore confirm major changes in Dantu RBC membranes, including a significant reduction in the *P. falciparum* invasion receptor, GYPA. To test whether these changes might explain reduced RBC invasion, we investigated invasion by a genetically modified *P. falciparum* strain in which *Pf*EBA175, the ligand for GYPA, had been disrupted[14]. The *Pf*EBA175-GYPA interaction is not essential for invasion, and when *Pf*EBA175 is deleted,

other invasion ligands can be transcriptionally up-regulated to compensate for the deletion phenotypically[14]. Invasion of Dantu RBCs by Δ*Pf*EBA175 parasites was also significantly reduced (**Fig. 2d, Supplementary Table 2**). Given that by definition, this parasite cannot use GYPA for invasion, the inhibitory impact of Dantu cannot entirely be explained by an altered *Pf*EBA175-GYPA interaction. Along with our earlier observations that Dantu decreases invasion both by strains known to rely heavily on *Pf*EBA175 (Dd2) and others that are less dependent on this pathway (3D7), this observation is further evidence that the impact of Dantu is not linked to specific receptor-ligand interactions.

Membrane tension is linked to invasion efficiency

To explore the broader RBC biomechanical effects of Dantu, we measured membrane contour fluctuations[16] by combining live imaging with flickering spectrometry[17] (**Extended Data Fig. 5**), enabling us to generate direct measurements of RBC membrane mechanics such as tension, radius, viscosity, and bending modulus. Tension and bending modulus represent the resistance of membranes to stretch and bend, respectively. Bending modulus is affected by lipid composition, membrane thickness, and membrane asymmetry while tension is set by osmotic pressure; the RBC cytoskeleton can affect both. These phenotypes vary naturally between RBCs, which can circulate for more than three months after they are produced from stem cells. As expected due to their lower MCV, Dantu RBCs had a significantly higher tension and smaller radius than non-Dantu RBCs, whereas no significant differences were seen in bending modulus and viscosity (**Fig. 3a**). The equatorial radius difference of 0.3 μm between non-Dantu and Dantu is minor, and likely explained by a shape change caused by the increased tension. Tension and radius are linked properties, higher tension leading directly to smaller RBCs (**Extended Data Fig. 6a**)[18].

To test for a link between tension and invasion, we measured both parameters simultaneously using video microscopy. Tension was measured for all RBCs adjacent to a rupturing schizont using high frame-rate capture (**Supplementary Video 4**), then the invasion fate of all parasite-RBC contact events with these same RBCs was monitored following schizont rupture (**Fig. 3b, Supplementary Video 5**). We observed an intrinsic distribution of membrane tensions in RBCs from each donor and discovered a clear association between tension and invasion: merozoites preferentially invaded neighbouring RBCs with low tension (**Fig. 3c, Supplementary Tables 5 and 6**). Comparing the distribution of tension values with invasion efficiency suggested a tension threshold for successful invasion that was consistent across all three genotype groups. The average of these tension thresholds across the genotype groups was 3.8 (±2.0) $*10^{-7}$ N/m, successful invasion being very rare above this threshold both in Dantu and non-Dantu RBCs (**Fig. 3c)**. Critically, the median tension was $8.2*10^{-7}$ N/m in Dantu RBCs, meaning that the majority were above the tension threshold of 3.8 (±2.0) $*10^{-7}$ N/m (**Fig. 3a**). The impact of Dantu on the biomechanical properties of the RBC is therefore sufficient to explain its impact on invasion, consistent with the invasion-inhibitory effect of Dantu being independent of a reliance on GYPs or other invasion receptors.

To probe the mechanism by which higher RBC membrane tension results in invasion resistance, we examined whether it impedes the merozoite's ability to wrap the RBC membrane around itself during invasion. Imaging at fine resolution established that parasites were considerably more wrapped by RBCs with lower membrane tensions (**Fig. 3d**). Consistent with this, there was also an association between tension and RBC deformation

during the invasion process, merozoite contacts with higher tension RBCs resulting in less RBC membrane deformation (**Extended Data Fig. 6b, Supplementary Table 6**).

We hypothesized that the molecular mechanism by which membrane tension is increased in Dantu RBCs might relate to changes in expression of membrane ion channels and in particular SLC9B2, a sodium-hydrogen exchanger that is upregulated in Dantu homozygous RBCs (**Fig. 2b**). Increased SLC9B2 expression could lead to increased intracellular sodium levels, overhydration and increase membrane tension. To test this hypothesis, we treated Dantu RBCs with phloretin, a broad-spectrum inhibitor of ion transporters. Phloretin resulted in decreased tension of both Dantu and non-Dantu RBCs (**Extended Data Fig. 7**), but unfortunately, it also inhibited egress of parasites from late-stage infected RBCs, making it impossible to test whether phloretin could rescue the invasion inhibitory effect of Dantu. As an alternative approach, we perturbed the membrane tension of non-Dantu RBCs by treating them with trace concentrations of glutaraldehyde, a compound that has been shown to increase RBC membrane tension without affecting bending modulus[22], and which therefore mimics the biophysical effect of Dantu. Treatment with 0.01% glutaraldehyde increased membrane tension in non-Dantu RBCs to levels that were similar to Dantu homozygous RBCs, and also caused a 43% reduction in invasion efficiency by 3D7 parasites (**Fig. 3e**). These data confirm the direct impact of RBC membrane tension on parasite invasion efficiency, independent of other parameters such as bending modulus.

In summary, we have established a mechanism whereby the complex structural polymorphism, Dantu, protects against severe malaria. We demonstrate a marked strain-transcending inhibition of *P. falciparum*-invasion into Dantu RBCs, and establish the novel

concept that it is the impact of Dantu on RBC membrane tension that mediates this inhibition, possibly via changes in the surface expression of membrane transporters that affect RBC hydration. By following, for the first time, tension and invasion at single-cell single-event resolution, we propose that irrespective of Dantu genotype, there is a tension threshold for successful *P. falciparum* invasion, a novel concept that links our understanding of RBC biomechanical properties[22,23] to the heterogeneity of parasite invasion. While previous studies have broadly linked invasion efficiency to RBC osmotic stress[19] and oxidative damage[20], both manipulations have multiple effects on RBC biomechanical properties, and can affect membrane deformability, rigidity, tension and bending modulus[20,21] (parameters defined in **Supplementary Table 7**). In this study, we were able to deconstruct these general biophysical membrane properties into specific components and demonstrate that it is altered tension, but not bending modulus or viscosity, that is associated with impaired invasion into Dantu RBCs.

The concept of a tension threshold potentially explains other well-established features of *P. falciparum* invasion, such as their preference for younger RBCs[24] which have lower tension and higher radii. Several other polymorphisms also affect RBC tension[25,26]; further studies will be required to investigate whether the same mechanism might be generalizable across multiple malaria-protective RBC traits. Membrane tension also changes with maturation of intracellular parasites[27,28], and in other contexts membrane tension has been implicated in the regulation of endocytosis[29] and the spreading of bacterial pathogens[30]. While improving our biological understanding of erythrocyte-parasite dynamics, this study also signals the potential for novel malaria interventions based on modifying the biomechanical properties of circulating RBCs.

References

1. MalariaGEN. Insights into malaria susceptibility using genome-wide data on 17,000 individuals from Africa, Asia and Oceania. *Nat Commun.* 2019;10(1):5732.
2. Williams TN. Host genetics. In: D. Gaur CECaVSC, ed. *Advances in Malaria Research.*2016.
3. Band G, Rockett KA, Spencer CC, Kwiatkowski DP. A novel locus of resistance to severe malaria in a region of ancient balancing selection. *Nature.* 2015;526(7572):253-257.
4. Ndila CM, Uyoga S, Macharia AW, et al. Human candidate gene polymorphisms and risk of severe malaria in children in Kilifi, Kenya: a case-control association study. *Lancet Haematol.* 2018.
5. Leffler EM, Band G, Busby GBJ, et al. Resistance to malaria through structural variation of red blood cell invasion receptors. *Science.* 2017;356(6343).
6. Sim BK, Chitnis CE, Wasniowska K, Hadley TJ, Miller LH. Receptor and ligand domains for invasion of erythrocytes by Plasmodium falciparum. *Science.* 1994;264(5167):1941-1944.
7. Mayer DC, Cofie J, Jiang L, et al. Glycophorin B is the erythrocyte receptor of Plasmodium falciparum erythrocyte-binding ligand, EBL-1. *Proc Natl Acad Sci U S A.* 2009;106(13):5348-5352.
8. Theron M, Cross N, Cawkill P, Bustamante LY, Rayner JC. An in vitro erythrocyte preference assay reveals that Plasmodium falciparum parasites prefer Type O over Type A erythrocytes. *Sci Rep.* 2018;8(1):8133.
9. Crick AJ, Theron M, Tiffert T, Lew VL, Cicuta P, Rayner JC. Quantitation of malaria parasite-erythrocyte cell-cell interactions using optical tweezers. *Biophys J.* 2014;107(4):846-853.
10. Weiss GE, Gilson PR, Taechalertpaisarn T, et al. Revealing the sequence and resulting cellular morphology of receptor-ligand interactions during Plasmodium falciparum invasion of erythrocytes. *PLoS Pathog.* 2015;11(2):e1004670.
11. Dahr W, Moulds J, Unger P, Kordowicz M. The Dantu erythrocyte phenotype of the NE variety. I. Dodecylsulfate polyacrylamide gel electrophoretic studies. *Blut.* 1987;55(1):19-31.
12. Maier AG, Duraisingh MT, Reeder JC, et al. Plasmodium falciparum erythrocyte invasion through glycophorin C and selection for Gerbich negativity in human populations. *Nat Med.* 2003;9(1):87-92.
13. Kanjee U, Gruring C, Chaand M, et al. CRISPR/Cas9 knockouts reveal genetic interaction between strain-transcendent erythrocyte determinants of Plasmodium falciparum invasion. *Proc Natl Acad Sci U S A.* 2017;114(44):E9356-e9365.
14. Reed MB, Caruana SR, Batchelor AH, Thompson JK, Crabb BS, Cowman AF. Targeted disruption of an erythrocyte binding antigen in Plasmodium falciparum is associated with a switch toward a sialic acid-independent pathway of invasion. *Proc Natl Acad Sci U S A.* 2000;97(13):7509-7514.
15. Cowman AF, Tonkin CJ, Tham WH, Duraisingh MT. The Molecular Basis of Erythrocyte Invasion by Malaria Parasites. *Cell Host Microbe.* 2017;22(2):232-245.

16. Betz T, Lenz M, Joanny JF, Sykes C. ATP-dependent mechanics of red blood cells. *Proc Natl Acad Sci U S A.* 2009;106(36):15320-15325.
17. Yoon YZ, Hong H, Brown A, et al. Flickering analysis of erythrocyte mechanical properties: dependence on oxygenation level, cell shape, and hydration level. *Biophys J.* 2009;97(6):1606-1615.
18. Popescu G, Ikeda T, Goda K, et al. Optical measurement of cell membrane tension. *Phys Rev Lett.* 2006;97(21):218101.
19. Tiffert T, Lew VL, Ginsburg H, Krugliak M, Croisille L, Mohandas N. The hydration state of human red blood cells and their susceptibility to invasion by Plasmodium falciparum. *Blood.* 2005;105(12):4853-4860.
20. Sinha A, Chu TT, Dao M, Chandramohanadas R. Single-cell evaluation of red blood cell bio-mechanical and nano-structural alterations upon chemically induced oxidative stress. *Sci Rep.* 2015;5:9768.
21. Evans E, Mohandas N, Leung A. Static and dynamic rigidities of normal and sickle erythrocytes. Major influence of cell hemoglobin concentration. *J Clin Invest.* 1984;73(2):477-488.
22. Koch M, Wright KE, Otto O, et al. Plasmodium falciparum erythrocyte-binding antigen 175 triggers a biophysical change in the red blood cell that facilitates invasion. *Proc Natl Acad Sci U S A.* 2017;114(16):4225-4230.
23. Sisquella X, Nebl T, Thompson JK, et al. Plasmodium falciparum ligand binding to erythrocytes induce alterations in deformability essential for invasion. *Elife.* 2017;6.
24. Pasvol G, Weatherall DJ, Wilson RJ. The increased susceptibility of young red cells to invasion by the malarial parasite Plasmodium falciparum. *Br J Haematol.* 1980;45(2):285-295.
25. Mohandas N, Lie-Injo LE, Friedman M, Mak JW. Rigid membranes of Malayan ovalocytes: a likely genetic barrier against malaria. *Blood.* 1984;63(6):1385-1392.
26. Schrier SL, Rachmilewitz E, Mohandas N. Cellular and membrane properties of alpha and beta thalassemic erythrocytes are different: implication for differences in clinical manifestations. *Blood.* 1989;74(6):2194-2202.
27. Park Y, Diez-Silva M, Popescu G, et al. Refractive index maps and membrane dynamics of human red blood cells parasitized by Plasmodium falciparum. *Proc Natl Acad Sci U S A.* 2008;105(37):13730-13735.
28. Park Y, Diez-Silva M, Fu D, et al. Static and dynamic light scattering of healthy and malaria-parasite invaded red blood cells. *J Biomed Opt.* 2010;15(2):020506.
29. Dai J, Ting-Beall HP, Sheetz MP. The secretion-coupled endocytosis correlates with membrane tension changes in RBL 2H3 cells. *J Gen Physiol.* 1997;110(1):1-10.
30. Lamason RL, Bastounis E, Kafai NM, et al. Rickettsia Sca4 Reduces Vinculin-Mediated Intercellular Tension to Promote Spread. *Cell.* 2016;167(3):670-683.e610.

Table and Figure Legends

Table 1 | Clinical and demographic characteristics of study participants.

Mean values for each clinical and demographic characteristic, with standard deviation (SD) in parentheses. n= 17 non-Dantu, 16 Dantu heterozygous and 13 Dantu homozygous individuals. Statistical comparison across genotypes was performed using the Kruskal-Wallis test, while pairwise comparisons between groups performed using Dunn's test. P adj* - adjusted for age, sex and multiple comparisons with Benjamini-Hochberg FDR adjustment. *$p < 0.05$.

Figure 1. Reduced invasion of Dantu variant RBCs by multiple *P. falciparum* strains. (a) The relative ability of *P. falciparum* strains from multiple geographic locations (3D7 and GB4 West Africa; Dd2 Southeast Asia; SA075 East Africa; 7G8 South America) to invade RBCs was measured using a flow cytometry-based preference invasion assay. The percentage of parasitised RBCs in each genotype group is indicated on the y-axis. Statistical comparison across groups was performed by one-way ANOVA, while pairwise comparisons between groups used the Tukey HSD test. Significant differences in invasion were observed between non-Dantu and Dantu homozygotes in 3D7 ($p=0.001$), Dd2 ($p=0.015$) and SAO75 ($p=0.028$). Statistical data listed in **Supplementary Table 2**. (**b**) The invasion process was also followed by live video microscopy, where the invasion rate of 3D7 merozoites was measured as the proportion of merozoites that contacted and successfully invaded RBCs, relative to all merozoites that contacted RBCs. Pre-invasion time - from first merozoite contact through RBC membrane deformation and resting; invasion time - from beginning of merozoite internalization to beginning of echinocytosis. 6 RBCs per genotype group were tested in both flow and video microscopy assays. In the video microscopy assays, the number of contacted

and successfully invaded RBCs counted were as follows: non-Dantu: 144/53, Dantu heterozygote: 191/43, Dantu homozygote: 233/41. Boxes indicate the median and interquartile ranges, while whiskers denote the total data range, with the dots outside the whiskers indicating the outliers. Bars show the mean and standard deviation of the video microscopy invasion data. Pairwise comparisons between genotypes were performed using the two-sided Mann-Whitney U test. **$p < 0.01$; *$p < 0.05$.

Figure 2. RBC membrane protein characteristics vary across Dantu genotypes but do not directly correlate with invasion efficiency. (a) The relative expression of essential RBC membrane proteins was assessed using fluorescent monoclonal antibodies in flow cytometry assays. 13 non-Dantu, 12 Dantu heterozygotes and 11 Dantu homozygotes were tested. Statistical comparison across groups was performed by one-way ANOVA, while pairwise comparisons between groups used the Tukey HSD test. Significant differences were observed in GYPA (non-Dantu vs. Dantu homozygote $p=6.25x10^{-11}$; non-Dantu vs. Dantu heterozygote $p= 4.62x10^{-6}$; Dantu heterozygote vs. Dantu homozygote $p= 6.86x10^{-4}$), GYPC (non-Dantu vs. Dantu homozygote p=0.03), Band3 (non-Dantu vs. Dantu homozygote $p=6.25x10^{-11}$; non-Dantu vs. Dantu heterozygote p=0.0136), CD71 (non-Dantu vs. Dantu homozygote p=0.006), and CR1 (non-Dantu vs. Dantu heterozygote p=0.003; Dantu heterozygote vs Dantu homozygote p=0.045). (**b**) Scatter plot of all proteins quantified by mass spectrometry (n=3 RBCs per genotype). Fold change was calculated by average signal:noise (Dantu homozygote/non-Dantu). GYPA was split into two parts: identified by peptides unique to GYPA ('GYPA unique', originating from extracellular region) or shared with the Dantu protein ('GYPA shared', originating from intracellular region). Mass spectra were processed with the quantitative proteomics platform "MassPike" and the method of significance A with

Benjamini-Hochberg multiple testing correction was used to estimate the p-value that each protein ratio was significantly different to 1. (**c**) Graph of the relative abundance of 'unique' and 'shared' GYPA peptides across all donors. Signal:noise values were normalised to a maximum of 1 for each protein. Statistical data for **(b)** and **(c)** listed in **Supplementary Table 4**. (**d**) Comparison of invasion efficiency of a genetically modified parasite strain, *ΔPfEBA175*, across genotypes (n=13 non-Dantu, 12 Dantu heterozygotes and 12 Dantu homozygotes) using the flow-cytometry-based preference invasion assay. The percentage of parasitised RBCs in each genotype is indicated on the y-axis. Statistical comparison across groups was by one-way ANOVA, while pairwise comparisons between groups used the Tukey HSD test (non-Dantu vs. Dantu homozygote p=0.04). ** $p < 0.01$; * $p < 0.05$.

Figure 3. Biomechanical properties of the RBC membrane differ across Dantu genotypes and correlate with invasion. (**a**) Membrane flickering spectrometry enabled measurement and comparison of RBC bending modulus, tension, radius, and viscosity across genotypes (n=6 RBCs per genotype). Mean and standard deviation were obtained from the averages of cell tensions for each sample: non-Dantu RBCs - (6.0 ±1.9) $*10^{-7}$ N/m; Dantu heterozygotes - (7.9±2.8) $*10^{-7}$ N/m; Dantu homozygotes - (8.8 ± 0.7) $*10^{-7}$ N/m. The impact of tension on parasite invasion was evaluated by simultaneously measuring tension from flickering analysis and live video imaging of the invasion process from rupturing schizonts ("egress", "deformation", then either "invasion" and "echinocytosis", or a failed invasion) (**b**), in non-Dantu and Dantu homozygote RBCs (**c**). The threshold range for tension, marked in (**a**) and (**c**), was obtained by comparing distributions of tension across Dantu genotypes with their invasion efficiency. (**d**) The contact region between merozoites and RBCs, represented in the snapshots, was measured during pre-invasion at the point of RBC maximum deformation for

2 sets of very high (n = 15) and low tension (n = 23) cells ($p=1.30 \times 10^{-32}$). Merozoite-RBC contact section was significantly smaller in high tension RBCs meaning that parasites were much more wrapped around RBCs with a lower membrane tension. (**e**) Parasite invasion efficiency and RBC tension for six increasing concentrations of glutaraldehyde (0.00001 - 0.01%). Parasite invasion was significantly decreased for RBC tensions around 8.8×10^{-7} N/m (22% decrease) and 12.2×10^{-7} N/m (43% decrease). Median values are reported from 2 technical replicates of 2 biologically independent samples. Pairwise comparisons between genotypes used the two-sided Mann-Whitney U test. ** $p < 0.01$. Number of cells and tension reported in **Supplementary Tables 5, and 6**.

Materials and Methods

Study participants. Samples were obtained from 42 children under the age of 13 years from two cohorts from the Kilifi County on the Indian Ocean coast of Kenya, who were involved in ongoing studies on malaria: (i) 18 children from a cohort subject to annual cross-sectional surveys through which blood samples are collected and frozen, and (ii) 24 children from a cohort recruited at 3-12 months of age and followed up for hospital admission since 2007, whose blood samples were collected and used in the assays within 24 hours of blood draw. Individual written informed consent was provided by the parents of all study participants. Ethical approval for the study was granted by the Kenya Medical Research Institute Scientific and Ethics Review Unit in Nairobi, Kenya (SERU3420 and SERU3500), the NHS Cambridgeshire 4 Research Ethics Committee (REC reference 15/EE/0253), and the Wellcome Sanger Institute Human Materials and Data Management Committee.

Genotyping Dantu samples. gDNA was extracted from whole blood using a QIAmp 96 DNA QIcube HT kit on a QIAcube HT System (QIAGEN) following manufacturer's instructions. The restriction fragment length polymorphism (RFLP) assay to detect genotypes at the Dantu marker SNP, rs186873296, has been previously described[4,5]. Briefly, PCR amplification of the region of interest containing rs186873296 was performed using the following primers: 5'ACGTTGGATGGCAGATTAGCATTCACCCAG3' and 5'ACGTTGGATGCTCCAGAGTAAGCATCCTTC3' generating an amplicon of 124bp. Fragmentation of the PCR product was then performed using the CviQI restriction enzyme (NEB), which allowed us to differentiate between non-Dantu homozygotes (AA) that would remain uncut, Dantu heterozygotes (AG) that would generate two bands of 64 and 56bp, and Dantu homozygotes (GG) which would generate a single band of 56bp.

***In vitro* culture of *P. falciparum* parasites.** All *P. falciparum* parasite strains used in this study (3D7, Dd2, SAO75, GB4, 7G8, ΔPfEBA175) were routinely cultured in human O-erythrocytes (NHS Blood and Transplant, Cambridge, UK, and Kenya Medical Research Institute, Nairobi, Kenya) at 3% hematocrit in RPMI 1640 medium with 25 mM Hepes, 20 mM glucose, and 25 µg/mL gentamicin containing 10% Albumax at 37°C (complete medium), under an atmosphere of 1% O_2, 3% CO_2, and 96% N_2 (BOC, Guildford, UK). Parasite cultures were synchronized on early ring stages with 5% D-sorbitol (Sigma-Aldrich, Dorset, UK). Use of erythrocytes from human donors for *P. falciparum* culture was approved by NHS Cambridgeshire 4 Research Ethics Committee and the Kenya Medical Research Institute Scientific and Ethics Review Unit.

RBC preference invasion assays. In all cases, blood was collected in EDTA-vacutainers and either used within 24h or cryopreserved using standard methods. Both fresh and frozen/thawed RBCs from Dantu homozygote, heterozygote and non-Dantu children were used in these assays, with no difference in parasite invasion efficiency being observed between them (**Extended Data Fig. 8**). RBCs were stained with three concentrations of CellTrace Far Red Cell Proliferation kit (Invitrogen, UK) - 1µM, 4µM and 16µM - corresponding to the three genotype groups. After a 2h incubation at 37°C under rotation, the stained RBCs were washed and resuspend to 2% Haematocrit (Hct) with complete medium. The cells were stored at 4°C until use for up to 24h after staining. To evaluate the preference of the parasites to invade RBCs of different Dantu genotype, parasite cultures containing mostly ring forms at 2-5% parasitaemia were pooled with equal volumes of RBCs from each genotype group (25µl pRBCs, 25µl Dantu homozygote RBCs, 25µl Dantu heterozygote RBCs and 25µl non-Dantu

RBCs) in the same well in 96-well plates. To evaluate whether the different concentrations of the dye could affect parasite growth, parasite cultures were mixed with stained RBCs from each genotype group in individual wells in a 1:1 ratio (50µl pRBCs + 50µl stained RBCs), while normal parasite growth controls were also evaluated by mixing parasite cultures with unstained RBCs from each genotype group in individual wells in a 1:1 ratio (50µl pRBCs + 50µl unstained RBCs). The samples were incubated for 48h at 37°C under static conditions as described above. After 48h, the cultures were treated with 0.5 mg/mL ribonuclease A (Sigma Aldrich, UK) in PBS for 1h at 37°C to remove any trace of RNA. To evaluate all parasitised RBCs, the cells were stained with 2x SYBR Green I DNA dye (Invitrogen, Paisley, UK) in PBS for 1 h at 37°C. Stained samples were examined with a 488nm blue laser, and a 633nm red laser on a BD FACS Canto flow cytometer (BD Biosciences, Oxford, UK). SYBR Green I was excited by a blue laser and detected by a 530/30 filter. CellTrace Far Red was excited by a red laser and detected by a 660/20 filter. BD FACS Diva software (BD Biosciences, Oxford, UK) was used to collect 50,000 events for each sample. The data collected were then further analysed with FlowJo (Tree Star, Ashland, Oregon) to obtain the percentage of parasitised RBCs within each genotype group. Statistical analyses were performed using R statistical software (version 3.3.3), where differences in invasion across the three Dantu genotype groups were evaluated using a one-way ANOVA test, while pairwise comparisons between genotype groups were evaluated using the Tukey HSD test. All experiments were carried out in triplicate and the data are presented as the median and interquartile ranges of invasion data across samples within each genotype group.

Live invasion imaging. All live imaging assays were performed blind to the Dantu genotype group. Highly concentrated (97-100%) infected cells (strain 3D7) were isolated by magnetic

separation (LD columns, Miltenyi Biotec, UK) directly before the experiments and re-suspended in complete medium either with Dantu or non-Dantu RBCs at 0.2 % Hct. The Dantu and non-Dantu RBCs suspensions were loaded in separate SecureSeal Hybridization Chambers (Sigma-Aldrich) and imaging was performed at the same time by employing 3 microscopes in order to guarantee the same conditions throughout the experiments. Each sample was recorded for about 2 hours to enable recording of a sufficient number of events. A custom-built temperature control system was used to maintain the optimal culture temperature of 37°C while running these experiments. Samples were placed in contact with a transparent glass heater driven by a PID temperature controller in a feedback loop with the thermocouple attached to the glass slide. A Nikon Eclipse Ti-E inverted microscope (Nikon, Japan) was used with a Nikon 60X Plan Apo VC N.A. 1.40 oil immersion objective, kept at physiological temperature through a heated collar. Motorised functions of the microscope were controlled via custom software written in-house and focus was maintained throughout the experiments using the Nikon "Perfect Focus system". Images were acquired in bright-field with red filter using a CMOS camera (model GS3-U3-23S6M-C, Point Grey Research/FLIR Integrated Imaging Solutions (Machine Vision), Ri Inc., Canada) at a frame rate of 4 fps, with pixel size corresponding to 0.0986 µm. We recorded one video for each egress-invasion event, from a few minutes before schizont rupture until the end of echinocytosis, around 20 minutes after egress. For each video, the duration of all the phases of an invasion process was assessed by two scientists independently, according to the following definitions of intervals: (i) 'pre-invasion' the time from the first evident contact between merozoite and RBC, throughout RBC deformation and subsequent resting; (ii) 'invasion' from the beginning of merozoite penetration of RBC throughout its complete internalisation until the beginning of echinocytosis; and finally (iii) 'echinocytosis' from the first curling of the RBC edge to the

recovery of its normal biconcave shape. Our measurements of invasion time are slightly longer than previous studies, which did not include the resting time from the end of parasite internalisation to the start of echinocytosis in their assessment of invasion time[10,31]. The parasite invasion efficiency or proportion of invasion has been quantified as the fraction of merozoites that contacted and successfully invaded RBCs divided by the number of all merozoites that contacted nearby RBCs post-egress, expressed as a percentage. This definition took into account the fact that in a chamber, we can have multiple invasions when more merozoites invade the same RBC. The degree to which merozoites deformed RBCs during invasion was given by a simplified four-point deformation scale (0, 1, 2, and 3), based on the most extreme degree of deformation achieved[10]. The visual assessment was done independently by two different experimentalists who were blinded to the genotypes of the RBCs in each video. We analysed six different RBC samples per genotype group, with data from 3 technical replicates. The total number of RBCs contacted by merozoites were: 155 for non-Dantu, 191 for Dantu heterozygotes, and 233 for Dantu homozygotes. The total number of successfully invaded cells were: 53 for non-Dantu, 43 for Dantu heterozygotes, and 41 for Dantu-homozygotes. The contact region between the merozoite and the RBC surface when the parasite deforms the host cell at its maximum was measured for 20 RBCs with both very high and very low tension from three different samples. Image thresholding filters (ImageJ) were used to distinguish the parasite and RBC contours from videos taken in bright-field at 100 fps. Only when merozoites were poised laterally to the RBC the thresholding process accurately identified them, and therefore only lateral invasions as in **Fig. 3d** were taken into account for this analysis. Both successful and failed invasions were considered, but as already reported in **Fig. 3c,** most RBCs with lower tension undergo a successful invasion, and vice versa.

Optical tweezers. The optical tweezers are built within the same Nikon inverted microscope used for imaging and consist of a solid-state pumped Nd:YAG laser (IRCL-2W-1064; CrystaLaser, Reno, NV) having 2W optical output at a wavelength of 1064 nm. The laser beam was steered via a pair of acousto-optical deflectors (AA Opto-Electronic, Orsay, France) controlled by custom-built electronics that allow multiple trapping with subnanometer position resolution. Videos were taken at 60 fps through a 60X Plan Apo VC 1.20 NA water objective (Nikon) with pixel size corresponding to 0.0973 µm. Dantu and non-Dantu RBCs were suspended in complete medium at 0.05 % Hct with purified schizonts and loaded in separate chambers coated with 10 µl solution of poly(l-lysine)-graft-poly(ethylene glycol) (PLL-g-PEG) (SuSoS AG, Dübendorf, Switzerland) at 0.5 mg/mL concentration and incubated for 30 minutes to prevent excessive adherence of cell proteins onto the coverslip. Adhesive forces at the merozoite-erythrocyte interface were quantified by evaluating the elastic morphological response of the erythrocyte as it resisted merozoite detachment[9]. Immediately after schizont egress, merozoites were manipulated by optical trapping and delivered to the surface of uninfected erythrocytes until attachment. Trapping durations were kept short (< 10 seconds) to minimise any possible detrimental effect of local heating: at full laser power, a few degrees Celsius of heating are expected locally around the laser beam focus. Then a second red blood cell was delivered close to the merozoite to form an erythrocyte-merozoite-erythrocyte system[9]. Erythrocyte maximal elongation before detachment was measured by pulling away the erythrocyte that adheres to the merozoite from their point of attachment, while the opposing force, on a second erythrocyte of our system, is given by either a second optical trap or by adhesion to the bottom of the sample chamber. We do not pull on the merozoite directly because this force would be weak and

difficult to calibrate. Finally, because erythrocytes are known to behave mechanically as a linear spring in this regime[32], the merozoite-erythrocyte adhesive forces were calculated by multiplying the erythrocyte end-to-end elongation before detachment and the stiffness of the erythrocyte cell. The experimentalist was blinded to the RBC genotype group.

Characterization of RBC membrane by flow cytometry. A panel of antibodies was selected against the 11 antigens that have been confirmed to be or could be potentially involved in cell adhesion and parasite invasion. Each blood sample was diluted at 0.5% haematocrit, washed twice with PBS and incubated in primary mouse monoclonal antibodies for 1h at 37°C. Antibodies used: anti-CD35-APC (CR1, Thermofisher, 1:50); antiCD44-BRIC 222-FITC (1:100, IBGRL); Integrin: anti-CD49d-APC (1:50, Milteny Biotec); anti-CD55-BRIC-216-FITC (1:500, IBGRL); Transferrin R: anti- CD71-FITC (1:100, ThermoFisher); Basigin: anti-CD147-FITC (1:100, ThermoFisher); Band3: anti-CD233-BRIC6-FITC (1:1000, IBGRL); Duffy antigen: anti-CD234-APC (1:100, Milteny Biotec); GYPA: CD235a-BRIC 256-FITC (1:1000, IBGRL); GYPC: anti-CD236R-BRIC10-FITC (1:1000, IBGRL). For detection of GYPB, first cells were incubated with an anti-GYPB (1:100, rabbit polyclonal antibody, Abcam), then washed twice with PBS and then incubated with a goat-anti-rabbit AlexFluor488 labelled antibody. After incubation, cells were washed twice in PBS and analyzed on a BD FACS Canto flow cytometer. Data were analyzed using FlowJo Software (Treestar, Ashland, Oregon). Statistical analyses to test differences in RBC membrane surface expression across genotype groups were performed using R statistical software (version 3.3.3).

Erythrocyte plasma membrane profiling. Plasma membrane profiling was performed as previously described[13]. Briefly, three of each Dantu genotype RBC samples were washed with

PBS. Surface sialic acid residues were oxidized with sodium meta-periodate (Thermo) then biotinylated with aminooxy-biotin (Biotium). After quenching, cells were incubated in 1% Triton X-100 lysis buffer. Biotinylated glycoproteins were enriched with high affinity streptavidin agarose beads (Pierce) and washed extensively. Captured protein was denatured with DTT, alkylated with iodoacetamide (IAA, Sigma) and digested on-bead with trypsin (Promega) in 200 mM HEPES pH 8.5 for 3h. Tryptic peptides were collected and labelled using TMT reagents. The reaction was quenched with hydroxylamine, and TMT-labelled samples combined in a 1:1:1:1:1:1:1:1:1 ratio. Labelled peptides were enriched, desalted, and 80% of the combined sample separated into twelve fractions using high pH reversed phase HPLC as previously described[33]. 100% of six fractions in addition to 50% of the remaining unfractionated sample were subjected to mass spectrometry.

Mass spectrometry data were acquired using an Orbitrap Fusion Lumos (Thermo Fisher Scientific, San Jose, CA) interfaced via an EASYspray source to an Ultimate 3000 RSLC nano UHPLC. Peptides were loaded onto a 100 µm ID x 2 cm Acclaim PepMap nanoViper precolumn (Thermo Fisher Scientific) and resolved using a 75 µm ID x 50 cm 2 µm particle PepMap RSLC C18 EASYspray column. Loading solvent was 0.1% FA, analytical solvent A: 0.1% FA and B: 80% MeCN + 0.1% FA. All separations were carried out at 40°C. Samples were loaded at 5 µL/minute for 5 minutes in loading solvent before beginning the analytical gradient. The following gradient was used: 3-7% solvent B over 2 minutes, 7-37% solvent B over 173 minutes, followed by a 4 minute wash at 95% solvent B and equilibration at 3% solvent B for 15 minutes. Each analysis used a MultiNotch MS3-based TMT method[34]. The following settings were used: MS1: 380-1500 Th, 120,000 Resolution, $2x10^5$ automatic gain control (AGC) target, 50 ms maximum injection time. MS2: Quadrupole isolation at an isolation width

of m/z 0.7, CID fragmentation (normalised collision energy (NCE) 35) with ion trap scanning in turbo mode from m/z 120, $1.5x10^4$ AGC target, 120 ms maximum injection time. MS3: In Synchronous Precursor Selection mode the top 10 MS2 ions were selected for HCD fragmentation (NCE 65) and scanned in the Orbitrap at 60,000 resolution with an AGC target of $1x10^5$ and a maximum accumulation time of 150 ms. Ions were not accumulated for all parallelisable time. The entire MS/MS/MS cycle had a target time of 3 s. Dynamic exclusion was set to +/- 10 ppm for 70 s. MS2 fragmentation was triggered on precursors $5x10^3$ counts and above.

Mass spectrometry data analysis. Mass spectra were processed using a Sequest-based software pipeline for quantitative proteomics, "MassPike", through a collaborative arrangement with Professor Steven Gygi's laboratory at Harvard Medical School. MS spectra were converted to mzXML using an extractor built upon Thermo Fisher's RAW File Reader library (version 4.0.26). In this extractor, the standard mzxml format has been augmented with additional custom fields that are specific to ion trap and Orbitrap mass spectrometry and essential for TMT quantitation. These additional fields include ion injection times for each scan, Fourier Transform-derived baseline and noise values calculated for every Orbitrap scan, isolation widths for each scan type, scan event numbers, and elapsed scan times. This software is a component of the MassPike software platform and is licensed by Harvard Medical School.

A combined database was constructed from the human Uniprot database (26th January, 2017) and common contaminants such as porcine trypsin and endoproteinase LysC. The combined database was concatenated with a reverse database composed of all protein

sequences in reversed order. Searches were performed using a 20 ppm precursor ion tolerance. Fragment ion tolerance was set to 1.0 Th. TMT tags on lysine residues and peptide N termini (229.162932 Da) and carbamidomethylation of cysteine residues (57.02146 Da) were set as static modifications, while oxidation of methionine residues (15.99492 Da) was set as a variable modification.

To control the fraction of erroneous protein identifications, a target-decoy strategy was employed[37]. Peptide spectral matches (PSMs) were filtered to an initial peptide-level false discovery rate (FDR) of 1% with subsequent filtering to attain a final protein-level FDR of 1%. PSM filtering was performed using a linear discriminant analysis, as described previously[35]. This distinguishes correct from incorrect peptide IDs in a manner analogous to the widely used Percolator algorithm (https://noble.gs.washington.edu/proj/percolator/), though employing a distinct machine learning algorithm. The following parameters were considered: XCorr, ΔCn, missed cleavages, peptide length, charge state, and precursor mass accuracy.

Protein assembly was guided by principles of parsimony to produce the smallest set of proteins necessary to account for all observed peptides (algorithm described in[35]. Proteins were quantified by summing TMT reporter ion counts across all matching peptide-spectral matches using “MassPike”, as described previously[34]. Briefly, a 0.003 Th window around the theoretical m/z of each reporter ion (126, 127n, 127c, 128n, 128c, 129n, 129c, 130n, 130c, 131n, 131c) was scanned for ions, and the maximum intensity nearest to the theoretical m/z was used. The primary determinant of quantitation quality is the number of TMT reporter ions detected in each MS3 spectrum, which is directly proportional to the signal-to-noise (S:N) ratio observed for each ion. Conservatively, every individual peptide used for quantitation

was required to contribute sufficient TMT reporter ions (minimum of ~1250 per spectrum) so that each on its own could be expected to provide a representative picture of relative protein abundance[34]. An isolation specificity filter with a cutoff of 50% was additionally employed to minimise peptide co-isolation[34]. Peptide-spectral matches with poor quality MS3 spectra (more than 8 TMT channels missing and/or a combined S:N ratio of less than 250 across all TMT reporter ions) or no MS3 spectra at all were excluded from quantitation. Peptides meeting the stated criteria for reliable quantitation were then summed by parent protein, in effect weighting the contributions of individual peptides to the total protein signal based on their individual TMT reporter ion yields. Protein quantitation values were exported for further analysis in Excel.

Proteins were filtered to include those most likely to be present at the cell surface with high confidence. These comprised proteins with Uniprot Subcellular Location (www.uniprot.org) terms matching 'Multipass', 'GPI anchored', 'Lipid Anchored', 'Type I transmembrane', 'Type II transmembrane', 'Type III transmembrane', 'Type IV transmembrane', and those predicted to have transmembrane regions based on TMHMM version 2.0[36].

For protein quantitation, reverse and contaminant proteins were removed. Despite extensive washing of biotinylated proteins when bound to Streptavidin beads, variable levels of contamination with abundant haemoglobin components were nevertheless detectable. As opposed to normalisation assuming equal protein loading across all channels, normalisation was instead performed from the summed signal:noise values of all proteins passing the filter described above. For further analysis and display in figures, only these filtered proteins are displayed. For **Fig. 2c** and **Extended Data Fig. 4b**, fractional TMT signals were used (i.e.

reporting the fraction of maximal signal observed for each protein in each TMT channel). For **Fig. 2b**, fold change was calculated on the basis of (average signal:noise (Dantu homozygote) / average signal:noise (non-Dantu). For figure **Extended Data Fig. 4a**, fold change was calculated for each Dantu variant donor by (signal:noise (Dantu homozygote) / average signal:noise (non-Dantu).

For **Fig. 2b**, the method of significance A was used to estimate the p-value that each protein ratio was significantly different to 1. Values were calculated and corrected for multiple hypothesis testing using the method of Benjamini-Hochberg in Perseus version 1.5.1.6[37]. For **Extended Data Fig. 4b**, two-tailed Student's t-test values were calculated and corrected for multiple hypothesis testing using the method of Benjamini-Hochberg in Excel. Hierarchical centroid clustering based on uncentered correlation was performed using Cluster 3.0 (Stanford University) and visualised using Java Treeview (http://jtreeview.sourceforge.net).

RBC membrane contour detection and flickering spectrometry. Dantu and non-Dantu RBCs were diluted into culture medium at 0.01% Hct and loaded in different chambers to provide an optimal cell density and avoid overlapping cells. All live-cell experiments were performed at 37°C by using the setup described above. 20 second time-lapse videos were recorded at high frame rate (514 frames/s) and short exposure time (0.8 ms). The RBC contour was detected in brightfield for each frame with subpixel resolution by an optimised algorithm developed in house and implemented in Matlab (The MathWorks, Natick, MA), as described previously[17] and in **Supplementary Section S1**. Full details of membrane fluctuation analysis are given in **Supplementary Section S2**. Briefly, the equatorial contour was decomposed into fluctuation modes by Fourier transforming to give a fluctuation power spectrum of mean

square mode amplitudes at the cell equator $\langle|h(q_x, y=0)|^2\rangle$ as a function of mode wavevector (q_x). From these data, the bending modulus (κ) and tension (σ) can be fitted using the following equation:

$$\langle|h(q_x, y=0)|^2\rangle = \frac{1}{L}\frac{k_B T}{2\sigma}\left(\frac{1}{q_x} - \frac{1}{\sqrt{\frac{\sigma}{\kappa}+q_x^2}}\right), \quad (1)$$

where k_B is the Boltzmann constant, *T* is temperature, and *L* is mean circumference of the RBC contour. This equation derives from the energy of deforming a flat sheet[38], and is a good description of shape fluctuations of the cell's equator only in a limited range of modes. We show in **Extended Data Fig. 10a,** through the calculus of the residues, that mode between 8 and 20 are well described by Eq. 1. Lower modes fail due to the closed shape of a cell, whereas higher modes fail due to optical and temporal resolution. This model considers fluctuations as having thermal origin. Eq. 1 has limiting behaviours as shown in a representative fluctuation power spectrum in **Supplementary Section S2**: the tension term (q^{-1} behavior) dominates at low modes while the bending modulus term (q^{-3} trend) dominates at high modes of the spectrum. In the range 8-20, for the parameters of RBCs, both terms contribute to Eq.1 and so both can be resolved robustly and independently, as demonstrated in **Extended Data Figs. 5 and 9**. The viscosity of RBCs was quantified by measuring the dynamics of the membrane fluctuations and their relaxation time for modes 7-11 (**Supplementary Section S2, Extended Data Fig. 10b**). This is a further independent check confirming the static study is measuring reliable values of tension (**Extended Data Fig. 10c**).

References for Materials and Methods

31. Gilson PR, Crabb BS. Morphology and kinetics of the three distinct phases of red blood cell invasion by Plasmodium falciparum merozoites. *Int J Parasitol.* 2009;39(1):91-96.

32. Yoon YZ, Kotar J, Yoon G, Cicuta P. The nonlinear mechanical response of the red blood cell. *Phys Biol.* 2008;5(3):036007.
33. Nightingale K, Lin KM, Ravenhill BJ, et al. High-Definition Analysis of Host Protein Stability during Human Cytomegalovirus Infection Reveals Antiviral Factors and Viral Evasion Mechanisms. *Cell Host Microbe.* 2018;24(3):447-460.e411.
34. McAlister GC, Nusinow DP, Jedrychowski MP, et al. MultiNotch MS3 enables accurate, sensitive, and multiplexed detection of differential expression across cancer cell line proteomes. *Anal Chem.* 2014;86(14):7150-7158.
35. Huttlin EL, Jedrychowski MP, Elias JE, et al. A tissue-specific atlas of mouse protein phosphorylation and expression. *Cell.* 2010;143(7):1174-1189.
36. Krogh A, Larsson B, von Heijne G, Sonnhammer EL. Predicting transmembrane protein topology with a hidden Markov model: application to complete genomes. *J Mol Biol.* 2001;305(3):567-580.
37. Cox J, Mann M. MaxQuant enables high peptide identification rates, individualized p.p.b.-range mass accuracies and proteome-wide protein quantification. *Nat Biotechnol.* 2008;26(12):1367-1372.
38. Pecreaux J, Dobereiner HG, Prost J, Joanny JF, Bassereau P. Refined contour analysis of giant unilamellar vesicles. Eur Phys J E Soft Matter. 2004;13(3):277-290.

Acknowledgements

We thank Emmanuel Mabibo, Jacob Golijo, Alphonse Kazungu, Ruth Mwarabu, the staff of Kilifi County Hospital and the KEMRI-Wellcome Trust Research Programme, Kilifi, for their help with participant recruitment, data and sample collection, and to Ellen Leffler and Gavin Band for discussions on the study. We also thank the study participants and their parents for agreeing to participate in this study. JCR, AM and DK were supported by the Wellcome Trust (206194/Z/17/Z). We acknowledge Virgilio Lew and Teresa Tiffert for generous provision of fresh blood and useful discussions. MPW is funded by a Wellcome Senior Fellowship (108070). TNW is funded through Fellowships awarded by the Wellcome Trust (091758 and 202800). SNK is supported by the Wellcome Trust-funded Initiative to Develop African Research Leaders (IDeAL) early-career postdoctoral fellowship (107769/Z/10/Z), supported through the DELTAS Africa Initiative (DEL-15-003). The Wellcome Trust provides core support to The KEMRI/Wellcome Trust Research Programme, Kilifi, Kenya (084535), Wellcome Sanger Institute, Cambridge, UK (206194/Z/17/Z) and the Wellcome Centre for Human Genetics,

Oxford, UK (090532/Z/09/Z, 203141). PC is supported by the Engineering and Physical Sciences Research Council (EPSRC) (EP/R011443/1), and VI is supported by the EPSRC and the Sackler fellowship. This paper is published with permission from the Director of KEMRI.

Author Contributions:

SNK, AMM, VI, BJR, YCL, MPW, PC, TNW and JCR conceived and planned the experiments. SNK and AMM carried out genotyping, RBC preference invasion and antibody characterization of RBC by flow cytometry; while VI and YCL performed live video imaging. VI carried out optical tweezers and erythrocyte membrane contour detection and flickering spectrometry. BJR performed the erythrocyte plasma membrane profiling. Each of the authors analysed the corresponding experiments. AM, JM, MT, and WN contributed to sample preparation and genotyping. JK, MC, JAR, KR and DK contributed to the interpretation of the results. All authors provided critical feedback and helped shape the research, analysis and manuscript.

Author Information:

All the authors declare neither financial nor non-financial competing interests. All correspondence should be addressed to any of the co-corresponding authors:

- Pietro Cicuta, Cavendish Laboratory, University of Cambridge, Cambridge CB3 0HE, United Kingdom. Phone: +44 1223 337462. E-mail: pc245@cam.ac.uk

- Thomas N. Williams, KEMRI/Wellcome Trust Research Programme, Centre for Geographic Medicine Research-Coast, Kilifi 80108, Kenya. E-mail: twilliams@kemri-wellcome.org

- Julian C. Rayner, Director, Cambridge Institute for Medical Research. Phone: +44 1223 762322. E- mail: jcr1003@cam.ac.uk

Data Availability

The authors declare that the data supporting the findings of this study are available within the manuscript and its Supplementary Information files.

Extended Data Figure Legends:

Extended Data Figure 1 | Erythrocytic cycle of malaria parasites. Illustration of the erythrocytic stage of the malaria parasite. **(a)** The merozoites undergo repeated rounds of asexual multiplication, progressing through ring, trophozoite and schizont stages. (1) This cycle starts when merozoites contact, attach and successfully invade RBCs in the circulation. The invasion period lasts for less than a minute and we are only able to follow the dynamics of such a fast event with real-time live microscopy[11,28]. The merozoite has a slightly ovoidal shape of 1 micron in diameter and is adapted for invasion of erythrocytes. The apical end of the parasite contains secretory organelles called rhoptries and micronemes that release proteins for helping merozoite's internalisation. In the host red cell, the parasite develops and multiplies, digesting haemoglobin, protected from immune attack. In the case of *Plasmodium falciparum*, the erythrocytic cycle lasts about 48 hours, and infected cells progress from (2) the ring stage (first 16 hours) throughout (3) trophozoite stage (around 16-36 hours) and, finally to (4) the schizont phase (lasts a few hours). The infected schizont then ruptures (5) releasing 15-30 daughter merozoites ready to infect new nearby red cells. In each cycle, less than 10% of parasites develop into the sexual form of the parasite called gametocytes (6). **(b)** Detailed illustration of the parasite invasion process into the red blood cell (1) described further in the Materials and Methods, involving the “pre-invasion” phase (contact, merozoite reorientation which triggers RBC membrane deformation, and tight attachment of the

merozoite to the RBC membrane), the “invasion” phase (initiation of invasion, penetration, complete internalization of the merozoite, and resealing of the RBC membrane), and the echinocytosis phase (formation of echinocyte). Icons adapted from ©biorender.com

Extended Data Figure 2 | Invasion process across Dantu genotype groups studied by time-lapse video microscopy. (a) RBC detachment force from a merozoite was measured using optical tweezers across genotype groups. RBCs attached to merozoites were pulled using optical traps, and the adhesive forces at the merozoite-RBC interface were quantified by evaluating the elastic morphological response of the RBC as it resisted merozoite detachment. Mean and standard deviation (SD) in **Supplementary Table 3.** Six biologically independent samples per genotype group were tested obtaining 21 events for non-Dantu, 19 for Dantu heterozygote, and 24 for Dantu homozygote. Importantly, the experimentalist was blinded to the RBC genotype group. The median is indicated by the middle red line in the boxplots, with the 25^{th} and 75^{th} percentiles indicated by the tops and bottoms of each plot, while whiskers denote total data range. If the median is not centered in the box, it shows sample skewness. Pairwise comparisons between genotype groups were performed using the two-sided Mann-Whitney U test. **(b)** The degree to which merozoites deformed RBCs during invasion was given by a simplified four-point deformation scale (0, 1, 2, and 3), based on the most extreme degree of deformation achieved (Weiss *et al*., *PLoS Pathog* 2015). The degree of deformation was compared across genotype groups with no significant difference noticed, and between successful and failed invasions. The percentage of RBCs undergoing strong deformations (score 2/3) is significantly higher in case of successful invasions, while RBCs that were contacted but not invaded experience weak deformations (score 0/1). Data from 155 cells for non-Dantu, 191 for Dantu heterozygote, and 233 for Dantu homozygote. Number of

successfully invaded cells: 53 for non-Dantu, 43 for Dantu heterozygote, and 41 for Dantu-homozygote. The visual assessment was done with blinded data by two different experimentalists. **(c)** Successful invasions are usually followed by a reversible echinocyte phase that lasts between 5 and 11 minutes (Gilson and Crabb, *Int J Parasitol*, 2009), until the recovery of newly infected RBC biconcave shape. The time of echinocytosis was in agreement with literature and not significantly different across genotype groups. Data from 53 cells non-Dantu, 43 Dantu heterozygote, and 41 Dantu-homozygote.

Extended Data Figure 3 | Distribution of reticulocytes and RNA concentrations across Dantu genotypes. Reticulocyte counts, and concentrations of RNA extracted from reticulocytes, were compared across Dantu genotypes. Reticulocyte count data was tested for 8 non-Dantu, 7 Dantu heterozygotes and 7 Dantu homozygote individuals, while RNA concentrations were measured in 9 non-Dantu, 7 Dantu heterozygotes and 7 Dantu homozygote individuals. The median is indicated by the middle red line in the boxplots, with the 25^{th} and 75^{th} percentiles indicated by the tops and bottoms of each plot, while whiskers denote total data range.

Statistical comparison across the three genotype groups was performed using a one-way ANOVA test, while all pairwise comparisons between genotype groups were performed using the Tukey HSD test correcting for multiple pairwise comparison tests using Benjamini-Hochberg FDR. Significant differences were observed in reticulocyte count (non-Dantu vs. Dantu homozygote $p=0.0023$) and RNA concentrations (non-Dantu vs. Dantu homozygote $p=0.0015$; non-Dantu vs. Dantu heterozygote $p=0.0088$). ** $p < 0.01$; * $p < 0.05$.

Extended Data Figure 4 | Plasma membrane profiling by tandem mass tag (TMT)-based MS3 mass spectrometry. The impact of the Dantu polymorphism on RBC membrane protein

expression levels was quantified using mass spectrometry. (**a**) Hierarchical cluster analysis of all proteins quantified and annotated as described in the Methods. Fold change was calculated for each donor by (signal:noise (donor) / average signal:noise (non-Dantu). (**b**) Proteomic quantification of markers shown in **Figure 2a** (3 biologically independent samples per genotype group). All markers were quantified by proteomics apart from GYPB. Statistical comparisons of quantitative protein expression across Dantu genotype groups were performed using two-tailed t-test with Benjamini-Hochberg multiple hypothesis correction: * p< 0.05, **p< 0.01. All p-values are listed in **Supplementary Table 4**.

Extended Data Figure 5 | Representative membrane fluctuation spectra for non-Dantu, Dantu heterozygous, and Dantu homozygous red blood cells. Example of contour detection and flickering spectra across genotype groups. (**a**) Contour of the RBC (dashed blue *line*), with inner and outer bounds used in image analysis (green lines). (**b**) Contour of the RBC. (**c)** Mean square fluctuation amplitudes for non-Dantu (green line), Dantu heterozygote (orange line), and Dantu homozygote (purple line) RBCs. Fitted modes 8-20.

The error bars (not shown for clarity) were calculated as $SD/\sqrt{(n \times dt)}$, where *SD* is the standard deviation, *n* total number of frames, and *dt* the time gap between frames.

Extended Data Figure 6 | Relationship between biophysical properties in non-Dantu and Dantu homozygote RBCs. (a) Scatter plot showing correlation between tension and radius in non-Dantu and Dantu homozygote RBCs. The shaded points in the background are all the data considered for non-Dantu (249) and Dantu (247) RBCs from six different biological replicates. The big marks in the foreground represent the mean and standard deviation in tension and radius of the six samples for non-Dantu and Dantu RBCs. There is a linear inverse relation

between radius and tension, where we observe that RBCs with higher tension have lower radii. Radius change is very small (0.3 μm) and, we believe, equatorial radius decrease is due to a shape change caused by the increased tension, and the two biophysical parameters have no different fluctuation modes. **(b)** The impact of tension on RBC deformation during pre-invasion, induced by merozoites contacting RBCs, was compared across Dantu genotype groups. RBCs having tension above the tension threshold tended to be weakly deformed (scores 0 and 1), whereas RBCs with tensions below the threshold were more strongly deformed (scores 2 and 3). Deformation scores as defined in Weiss *et al*. *PLoS Pathog.* 2015 (Reference 10 of the manuscript).

Extended Data Figure 7 | Reduction of membrane tension both in non-Dantu and Dantu homozygous RBCs with phloretin. Biophysical properties in non-Dantu (**a,b**) and Dantu homozygous (**c,d**) RBCs after phloretin treatment **p < 0.01. Phloretin treatment causes a decrease in tension without affecting bending modulus at 150 (p = 0.0015) and 200 (p = 1.72 $x10^{-4}$) μM for both non-Dantu and Dantu samples. Above 200 μM concentration of phloretin, most RBCs become crenated and cannot be used for flickering spectroscopy. Phloretin has an effect on RBC tension only when it is present in the medium, i.e. RBCs recover their normal tension when washed. (**a-b**) Data from about 30 cells from 3 biologically independent non-Dantu samples. **(c-d)** Data from 60 cells from 4 biologically independent Dantu samples. Between untreated and phloretin 150 μM (p = 0.01) and between untreated and phloretin 200 μM (p = 0.0022) using the two-sided Mann-Whitney U test.

Extended Data Figure 8 | Comparing parasite invasion and biomechanical properties of frozen and fresh RBCs.

Comparison of parasite invasion efficiency and biomechanical properties in frozen vs fresh RBCs. (**a**) The invasion efficiency of *P. falciparum* laboratory strain, 3D7, was compared across frozen and fresh RBCs (n=6 frozen and n=14 non-Dantu, 12 Dantu heterozygote and 12 Dantu homozygote fresh biologically independent RBC samples per genotype group were tested). The percentage of parasitised RBCs that successfully invaded each genotype group was measured using a flow cytometry-based invasion assay. Boxplots indicate the median (middle line) and interquartile ranges (top and bottom of boxes) of the data, while whiskers denote the total data range. Statistical comparison across the three genotype groups was performed using a one-way ANOVA test, while pairwise comparisons between genotype groups were performed using the Tukey HSD test, with significant differences in 3D7 invasion observed in frozen RBCS (non-Dantu vs. Dantu homozygote p=0.001) and in fresh RBCs (non-Dantu vs. Dantu homozygote p=0.001). **p < 0.01; *p < 0.05. (**b**) Membrane flickering spectrometry enabled measurement of RBC biomechanical properties (bending modulus, tension, radius, and viscosity) of fresh (n = 53) and frozen (n = 51) RBCs from the same donor. No statistically significant differences were detected between the two conditions for all the measured biophysical properties. Pairwise comparisons were performed using the two-sided Mann-Whitney U test; p Bending modulus = 0.1, p Tension = 0.6, p Radius = 0.7, p Viscosity = 0.6.

Extended Data Figure 9 | Decoupling tension and bending modulus with flickering analysis. To test our ability to decouple tension and bending modulus from our data through the flickering analysis, we have taken the 20 highest tension and the 20 lowest tension cells from our database and shown that on analysing the fluctuation power spectra of these, which cover a wide enough range of q-values that both tension and bending moduli can be robustly extracted. (**a-b**) Boxplots for the tensions and bending moduli of the 20 cells with extreme

high and extreme low tensions. While there is an obvious significant difference in tension ($p=4.0302 \times 10^{-13}$, two-sided Mann-Whitney U test), bending modulus is similar. (**c**) This is also evident from the overlapping of the two spectra for the high modes where a bending-dominated regime prevails, whereas the divergence of the fluctuation amplitudes between the two spectra becomes noticeable when tension predominates. Each mean-square fluctuation spectrum is obtained averaging all 20 fluctuation spectra for both low (blue) and high (yellow) tension cells. Since tension dominates low modes (q^{-1} behavior) and bending modulus dominates high modes of the spectra (q^{-3} trend), the decoupling between tension and bending modulus becomes evident from these two spectra (**Extended Data Section S2**).

Extended Data Figure 10 | Membrane flickering spectroscopy amplitude analysis. (a) To justify our choice of modes for fitting **Eq. S4**, we calculated the residuals of mean square fluctuation amplitudes at different ranges of modes for the same RBC. The figure shows that the residues derived from fitting modes above 20 increase steadily, suggesting a systematic error in fitting modes above 20. Our range of modes (8-20) seems the most convincing range, as well as range 5-20, with no systematic deviations.

By studying the dynamics of modes it is possible to extract the viscosity of the cell interior, and this analysis can be used as further proof of the method. From the timescale of decorrelation of mode amplitudes, it is possible to obtain the viscosity of the RBC interior, using the values of tension and bending modulus obtained from the static spectrum of the same cell. This is achieved by fitting the relaxation time with **Eq. S7**. The viscosity is statistically the same, across the non-Dantu and Dantu groups which have statistically different tension values. This is thus a further independent check confirming the static study is measuring tension values reliably. **(b)** The viscosities of RBCs with extreme low and high tension are not

significantly different (p value=0.14, two-sided Mann-Whitney U test). The fit in the inset shows data from one of the RBCs in the sample. **(c)** The relaxation times, plotted vs q_x, modes 5-11, are represented for both the low- and high-tension RBCs; the trend is 1/q consistent with the limiting behaviour of **Eq. S7** for ($\sigma \gg \kappa q_x^2$). The range of modes that can be studied dynamically is limited by the camera acquisition rate, as well as by the other factors that limit also the static analysis.

Table 1 | Clinical and demographic characteristics of study participants

					Pairwise comparisons between genotype groups		
Characteristic	**non-Dantu**	**Dantu Heterozygote**	**Dantu Homozygote**	**P adj (Comparison across genotype groups)**	**P adj *(non-Dantu vs. Dantu Heterozygote)***	**P adj *(non-Dantu vs. Dantu Homozygote)***	**P adj *(Dantu Heterozygote vs. Dantu Homozygote)***
Mean Age (SD; years)	11.4 (1.6)	11.6 (1.7)	9.3 (4.1)	-	0.3671	0.1498	0.1704
Sex (F/M)	5/10	5/9	5/8	-	0.4557	0.9064	0.5127
Red blood cell count (SD; $10^6/\mu L$)	4.60 (0.36)	4.62 (0.34)	4.94 (0.68)	0.286	0.3538	0.1743	0.1897
Reticulocyte count (SD; $10^6/\mu L$)	0.02 (0.01)	0.04 (0.01)	0.05 (0.02)	0.545	0.4451	0.4539	0.2906
White blood cell count (SD; $10^3/\mu L$)	5.83 (1.46)	5.67 (0.78)	6.89 (2.93)	0.643	0.3684	0.5249	0.407
Platelet count (SD; $10^3/\mu L$)	284.06 (77.91)	293.31 (73.91)	346.92 (96.40)	0.106	0.3112	0.0594	0.087
Haematocrit (SD; %)	37.23 (1.66)	37.23 (2.68)	36.22 (2.42)	0.188	0.419	0.0959	0.1357
Haemoglobin concentration (SD; g/dL)	12.54 (0.54)	12.59 (0.93)	12.08 (1.13)	0.168	0.3615	0.1029	0.1085
Mean cell volume (SD; fL)	81.32 (4.69)	80.78 (4.67)	74.40 (9.66)	0.015*	0.344	0.0094*	0.0152*
Mean cell haemoglobin (SD; pg)	27.38 (1.75)	27.31 (1.83)	24.90 (4.12)	0.015*	0.454	0.0131*	0.0099*
Mean cell haemoglobin concentration (SD; g/dL)	33.67 (0.60)	33.81 (0.63)	33.33 (1.51)	0.113	0.2774	0.0986	0.0622
Red blood cell distribution width (SD; %)	12.83 (1.29)	12.70 (1.13)	13.78 (1.66)	0.830	0.4987	0.88	0.4452

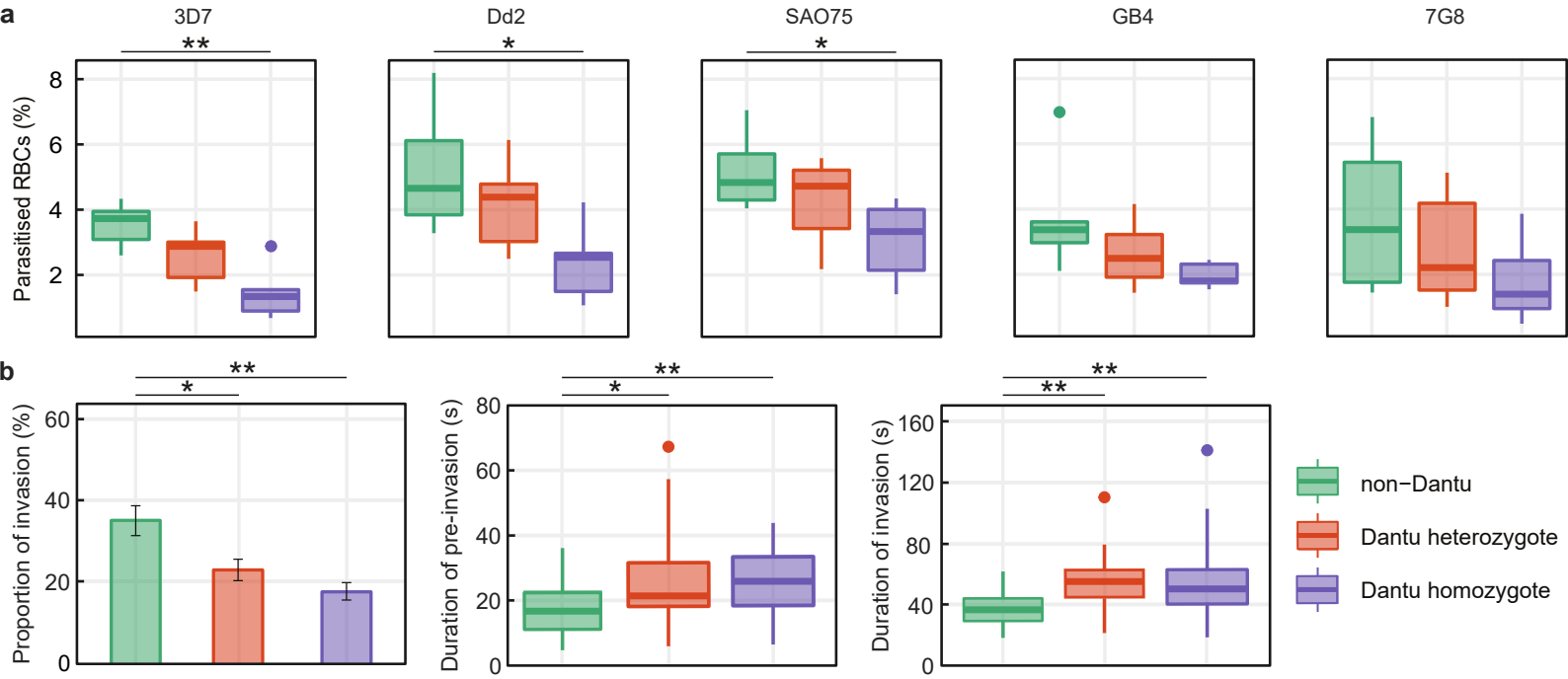
a
3D7
Dd2
SAO75
GB4
7G8
Parasitised RBCs (%)
b
Proportion of invasion (%)
Duration of pre-invasion (s)
Duration of invasion (s)
non−Dantu
Dantu heterozygote
Dantu homozygote

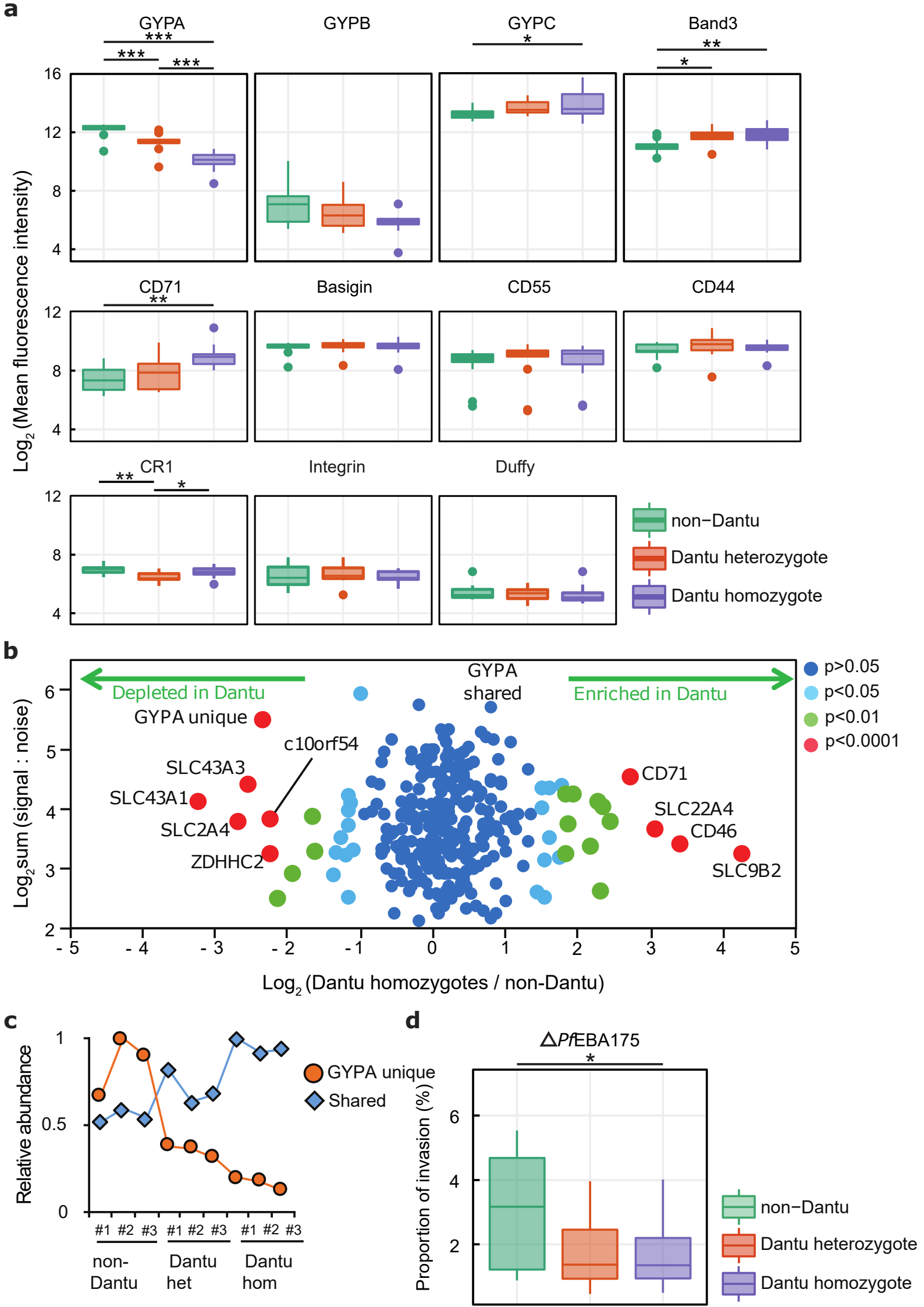
a
GYPA
GYPB
GYPC
Band3
CD71
Basigin
CD55
CD44
CR1
Integrin
Duffy
Log2 (Mean fluorescence intensity)
non−Dantu
Dantu heterozygote
Dantu homozygote
b
Depleted in Dantu
Enriched in Dantu
GYPA unique
GYPA shared
c10orf54
SLC43A3
SLC43A1
SLC2A4
ZDHHC2
CD71
SLC22A4
CD46
SLC9B2
p>0.05
p<0.05
p<0.01
p<0.0001
Log2sum (signal : noise)
Log2 (Dantu homozygotes / non-Dantu)
c
Relative abundance
GYPA unique
Shared
non-Dantu
Dantu het
Dantu hom
d
ΔPfEBA175
Proportion of invasion (%)
non−Dantu
Dantu heterozygote
Dantu homozygote

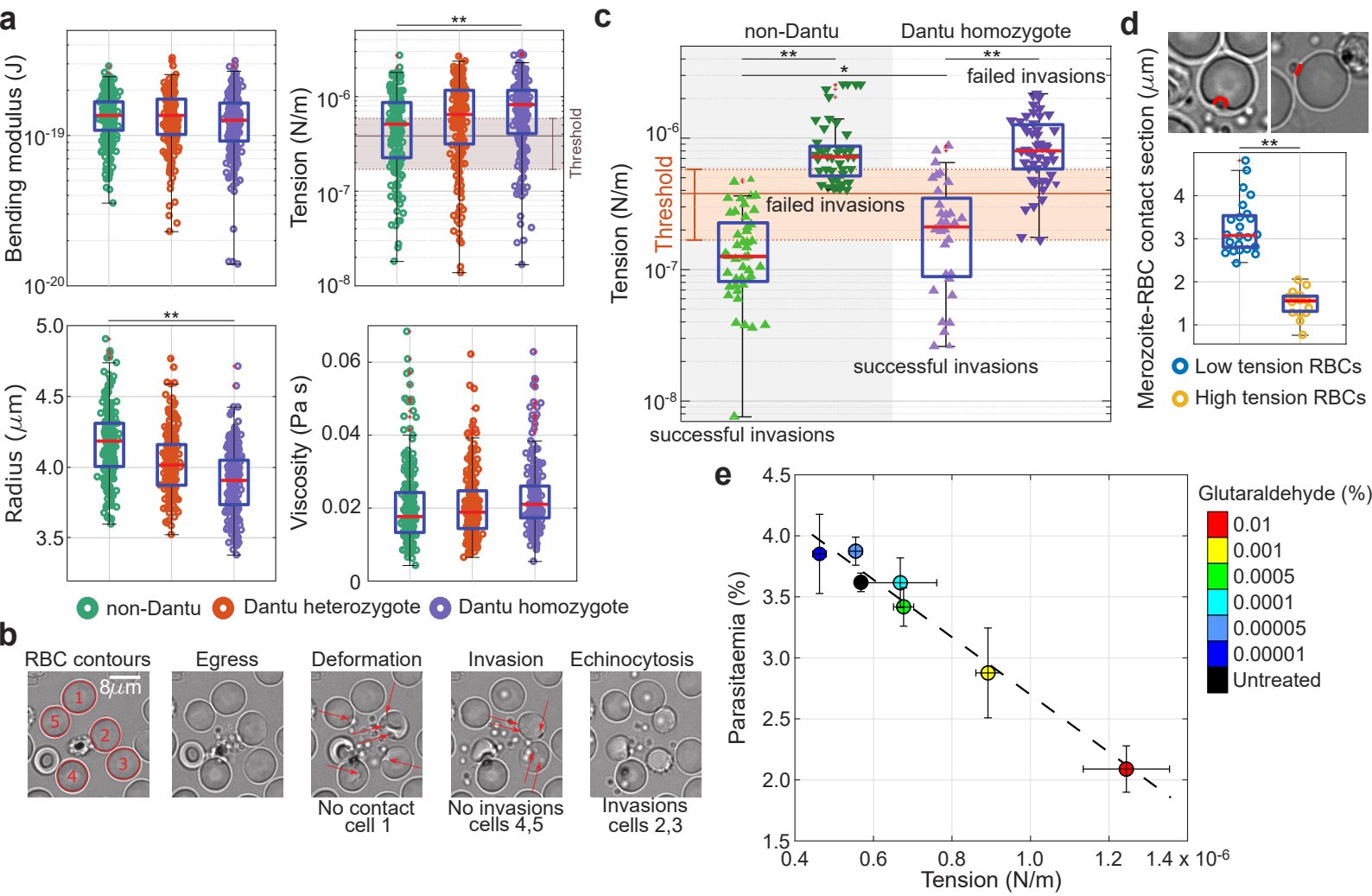
a
Bending modulus (J)
Tension (N/m)
Threshold
Radius (μm)
Viscosity (Pa s)
non-Dantu
Dantu heterozygote
Dantu homozygote
b
RBC contours
Egress
Deformation
Invasion
Echinocytosis
8μm
No contact cell 1
No invasions cells 4,5
Invasions cells 2,3
c
non-Dantu
Dantu homozygote
failed invasions
Threshold
successful invasions
d
Merozoite-RBC contact section (μm)
Low tension RBCs
High tension RBCs
e
Parasitaemia (%)
Tension (N/m)
Glutaraldehyde (%)
0.01
0.001
0.0005
0.0001
0.00005
0.00001
Untreated

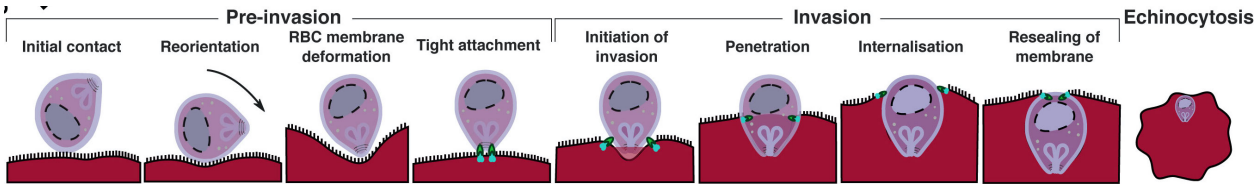
Pre-invasion
Invasion
Echinocytosis
Initial contact
Reorientation
RBC membrane deformation
Tight attachment
Initiation of invasion
Penetration
Internalisation
Resealing of membrane

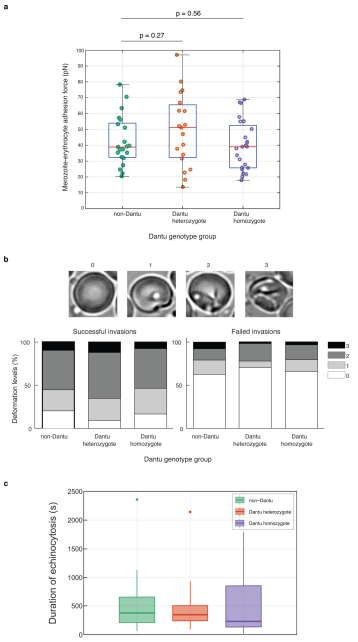
a
p = 0.56
p = 0.27
Merozoite-erythrocyte adhesion force (pN)
non-Dantu
Dantu heterozygote
Dantu homozygote
Dantu genotype group
b
0
1
2
3
Successful invasions
Failed invasions
Deformation levels (%)
non-Dantu
Dantu heterozygote
Dantu homozygote
Dantu genotype group
c
Duration of echinocytosis (s)
non-Dantu
Dantu heterozygote
Dantu homozygote

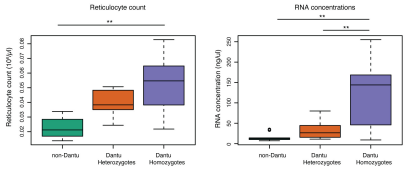
Reticulocyte count
**
Reticulocyte count (10^9/µl)
0.02
0.03
0.04
0.05
0.06
0.07
0.08
non-Dantu
Dantu Heterozygotes
Dantu Homozygotes
RNA concentrations
**
**
RNA concentration (ng/µl)
0
50
100
150
200
250
non-Dantu
Dantu Heterozygotes
Dantu Homozygotes

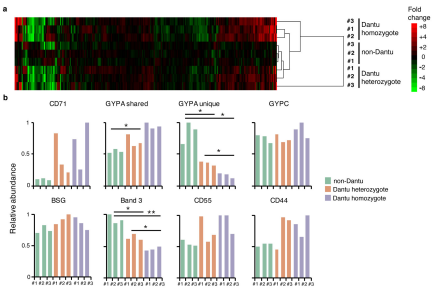
a
Fold change
+8
+4
+2
0
-2
-4
-8
#3
#1
#2
Dantu homozygote
#3
#2
#1
non-Dantu
#1
#2
#3
Dantu heterozygote
b
CD71
GYPA shared
GYPA unique
GYPC
BSG
Band 3
CD55
CD44
Relative abundance
non-Dantu
Dantu heterozygote
Dantu homozygote

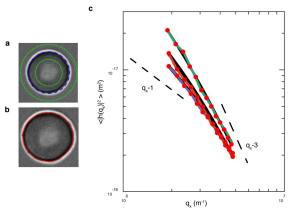
a
b
c
q_r-1
q_r-3
q_r (m^{-1})

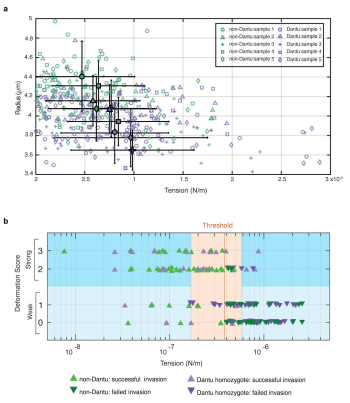
a
non-Dantu sample 1
non-Dantu sample 2
non-Dantu sample 3
non-Dantu sample 4
non-Dantu sample 5
Dantu sample 1
Dantu sample 2
Dantu sample 3
Dantu sample 4
Dantu sample 5
Radius (μm)
Tension (N/m)
3 x10⁻⁴
b
Threshold
Deformation Score
Strong
Weak
Tension (N/m)
non-Dantu: successful invasion
non-Dantu: failed invasion
Dantu homozygote: successful invasion
Dantu homozygote: failed invasion

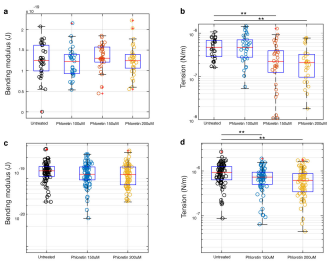
a
b
c
d
Bending modulus (J)
Tension (N/m)
Unheated
Pilocrebo 100uM
Pilocrebo 200uM
**

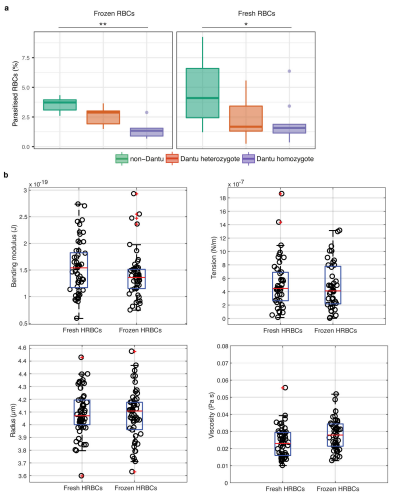
a
Frozen RBCs
++
Fresh RBCs
*
Percentage of RBCs (%)
non−Dantu
Dantu heterozygote
Dantu homozygote
b
Bending modulus (J)
Fresh HRBCs
Frozen HRBCs
Tension (N/m)
Radius (μm)
Viscosity (Pa·s)

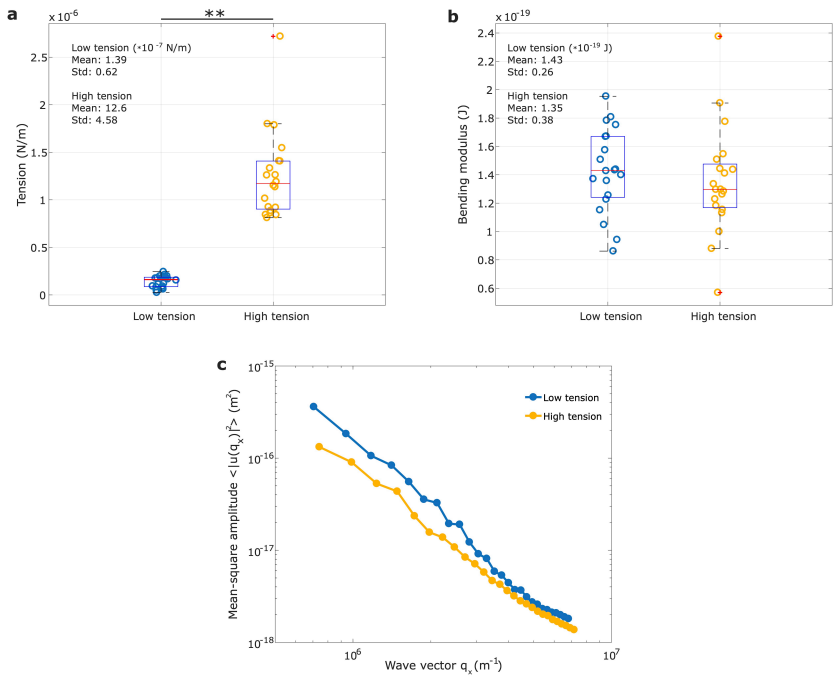
a
x 10^-6
**
Low tension (×10^-7 N/m)
Mean: 1.39
Std: 0.62
High tension
Mean: 12.6
Std: 4.58
Tension (N/m)
2.5
2
1.5
1
0.5
0
Low tension
High tension
b
x 10^-19
Low tension (×10^-19 J)
Mean: 1.43
Std: 0.26
High tension
Mean: 1.35
Std: 0.38
Bending modulus (J)
2.4
2.2
2
1.8
1.6
1.4
1.2
1
0.8
0.6
Low tension
High tension
c
Low tension
High tension
Mean-square amplitude <|u(q_x)|^2> (m^2)
10^-15
10^-16
10^-17
10^-18
10^6
10^7
Wave vector q_x (m^-1)

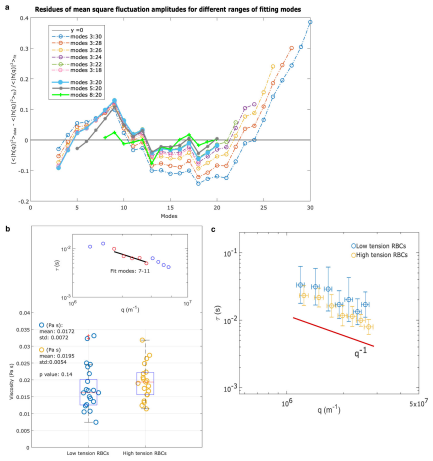
a
Residues of mean square fluctuation amplitudes for different ranges of fitting modes
γ =0
modes 3:30
modes 3:28
modes 3:26
modes 3:24
modes 3:22
modes 3:18
modes 3:20
modes 5:20
modes 8:20
Modes
b
Fit modes: 7-11
q (m⁻¹)
Low tension RBCs
High tension RBCs
c
Low tension RBCs
High tension RBCs
q⁻¹
q (m⁻¹)

Supplementary Information

Supplementary material to Nature manuscript 2018-11-16415: " **Red blood cell tension protects against severe malaria in the Dantu blood group** ".

Authors: Silvia N. Kariuki*, Alejandro Marin-Menendez*, Viola Introini*, Benjamin J. Ravenhill, Yen-Chun Lin, Alex Macharia, Johnstone Makale, Metrine Tendwa, Wilfred Nyamu, Jurij Kotar, Manuela Carrasquilla, J. Alexandra Rowe, Kirk Rockett, Dominic Kwiatkowski, Michael P. Weekes, Pietro Cicuta*, Thomas N. Williams*, Julian C. Rayner*.

Supplementary Methods

S1: Theoretical basis of membrane flickering spectroscopy

Flickering spectroscopy is a technique that allows the extraction of information about the mechanical properties of a fluctuating membrane through an analysis of its thermal fluctuations.

The classical derivation of the membrane fluctuation spectrum as formulated by Helfrich *et al*.[1] is valid for small fluctuations in a quasi-planar approximation, assuming fluctuations are of thermal origin[2,3,4,5,9]. The expression for the elastic energy *E* required to deform a flat membrane to a shape given by *h(x,y)*, when resisted by a membrane tension and a bending modulus, is

$$E = \frac{1}{2}\int dxdy\left\{\kappa(\nabla^2 h(x,y))^2 + \sigma\left(\vec{\nabla}h(x,y)\right)^2\right\}, \quad \text{(S.1)}$$

where σ is the tension, κ the bending modulus, and $h(x,y)$ the height of the membrane with respect to a fixed horizontal plane in the point of coordinates (x,y). Membrane tension is defined as the resistance to stretch and in a red blood cell it is primarily provided by the cytoskeleton and by osmotic pressure. Bending modulus is an intrinsic property of the membrane, related to the amount of energy required to bend it; it is affected by lipid composition, membrane thickness, cytoskeleton, membrane asymmetry, but not by osmotic pressure.

If the membrane considered is squared with dimension $L \times L$ and with periodic boundary conditions it is possible to expand $h(x,y)$ using Fourier series and, following[6], to obtain

$$E = L^2 \sum_{\vec{q}} |h(\vec{q})| \left\{\frac{1}{2}\kappa q^4 + \frac{1}{2}\sigma q^2\right\}. \quad \text{(S.2)}$$

where the wavevectors *q* are $(q_x + q_y)^{½}$, with q_x and q_y as usual in the set 2pi/*L*i, i=1:inf. This expression shows that a fluctuation mode will cost either more bending or more stretching energy depending on the wave vector: for small wave vectors, i.e. large length scales, the energy cost will be mainly due to stretching and for bigger wave vectors bending will dominate instead. Using the equipartition theorem, the mean square amplitude of each mode can be related to the bending modulus and tension by

$$\langle |h(\vec{q})|^2 \rangle = \frac{k_B T}{L^2(\kappa q^4 + \sigma q^2)}. \quad \text{(S.3)}$$

The angular brackets denote an ensemble average (in experiments, a time average), k_B the Boltzmann's constant and T the absolute temperature. Equation S.3 is the expression for the fluctuation spectrum of the membrane, hence, the mean square amplitude of the modes depends on the thermal energy and on

the membrane properties. This quantity is central for the flickering spectroscopy analysis which consists in measuring the mean square amplitude of the modes of a fluctuating membrane and then fitting the experimental spectrum with equation S.3 to obtain tension and bending modulus.

Pecreaux *et al*.[7] demonstrated that the planar approximation can still be adapted in the case of closed objects such vesicles, where only the fluctuations of the cell in the plane of its equator (*y*=0) are considered. The resulting contour fluctuations can be calculated by an inverse Fourier-transform over q_y of Eq. S.3, evaluated for $y = 0$:

$$\langle \left| h\left(q_x, y = 0\right) \right|^2 \rangle = \frac{k_B T}{L} \frac{1}{2\sigma} \left(\frac{1}{q_x} - \frac{1}{\sqrt{\frac{\sigma}{\kappa} + q_x^2}} \right). \tag{S.4}$$

A red blood cell membrane is much more complex than a simple phospholipid bilayer and its fluctuations could be considered as constrained by the spectrin skeleton[10]. This can be addressed with a tethering parameter γthat links lipids to cytoskeleton, and in this case, the expression of the fluctuations is[2]

$$\langle \left| h\left(q_x, y = 0\right) \right|^2 \rangle = \\ = \frac{k_B T}{L} \sqrt{\frac{\kappa}{2(\sigma^2 - 4\kappa\gamma)}} \left[\frac{1}{\sqrt{2\kappa q_x^2 + \sigma - \sqrt{\sigma^2 - 4\kappa\gamma}}} - \frac{1}{\sqrt{2\kappa q_x^2 + \sigma + \sqrt{\sigma^2 - 4\kappa\gamma}}} \right], \tag{S.5}$$

where γ is the constraining term or elastic restoring force.
We discuss below the range of modes that can be addressed experimentally, which is the most important limitation of this approach. An alternative experimental technique of beam deflection, Betz *et al*.[8,11] has suggested an ATP-dependent mechanics of red blood cells, but this has not been confirmed in other contour flickering experiments[4,5,9] and thus we believe that it is appropriate to analyse the equatorial fluctuations of RBCs using equations S.4 and S.5.

S2: Membrane contour detection algorithm and flickering amplitude analysis

The flickering method relies on image analysis of detailed shapes of the RBC. In particular, the equatorial profile can be detected very accurately with sub-pixel resolution from digital video recordings, and analysed automatically as published in previous works[2].
Each cell was recorded in bright field for 10000 frames at 514 frames/s with 0.8 ms of exposure time. The exposure time was set as short as possible to increase the range of modes that can be analysed; in fact modes with a lifetime shorter than the exposure time will be integrated and therefore not be considered. From each digital frame, we extracted the resulting radial profile $r(\phi)$, where r is the radius of the cell equator and ϕ is the azimuthal angle (from 0 to 360 degrees). The information from the whole image stack is analysed to determine mechanical and dynamical parameters of the cell, as described below and in Yoon *et al*. These profiles are then Fourier transformed and the mean square amplitude of each Fourier

mode is calculated. This amplitude can be fitted to Eq. S.5, which is derived from the theory of fluctuations described above. In our data, we do not see an effect of gamma, whereas sigma and kappa can be robustly fitted. The amplitudes of very low modes <5 (large wavelength) are excluded because they are affected by the geometry of the surface and because the deviation from the exact spherical harmonics expression becomes significant. Very high modes (> 20) are affected by noise and their fluctuations lie outside the spatial and temporal resolution of the experiment. This is validated in **Fig.S15**. We thus considered modes 8 to 20 for fitting to the theory. Examples of our spectra are reported in **Supplementary Fig. 9**.

Eq. S.4 has two limiting behaviours: $\langle h\left(q_x, y=0\right)^2\rangle \sim q^{-1}$ for low modes, if dominated by tension ($\sigma \gg \kappa q_x^2$); Instead, at large *q*, there is a bending-dominated regime $\langle h\left(q_x, y=0\right)^2\rangle \sim q^{-3}$ for ($\sigma \ll \kappa q_x^2$). In the range we consider, which is the whole experimentally accessible range, both terms are contributing to the deformation energy, and the slope is an intermediate power law. This is fortunate, because it means that this approach is able to address both tension and bending, for red blood cells.

The dynamics of the fluctuations can also be quantified[2]. We calculated the autocorrelation function of the modes, averaged over 10000 frames. This analysis works well on modes 7 to 11, but higher modes decay too fast to be fitted. The range of modes that can be studied dynamically is limited by the camera acquisition rate, as well as by the other factors that limit also the static analysis.

The time correlation function of spatial modes is an exponential decay:

$$C_{\vec{q}}(t) = \langle h(\vec{q}, t'), h\left(\vec{q}, t' + t\right)\rangle_{t'}, \tag{S.6}$$

where the timescale is $\tau_{\vec{q}}$ in general given by

$$\frac{1}{\tau_{\vec{q}}} = \frac{2\gamma + \sigma q^2 + \kappa q^4}{2\left(\frac{\eta_M}{R^2} + q\eta_{int} + q\eta_{ext}\right)}. \tag{S.7}$$

Equation S.7 gives the relaxation timescale of the modes of a two-dimensional membrane, as a function of the wave vectors. In Eq. S.7, η_M is the two-dimensional membrane viscosity, η_{int} and η_{ext} are the viscosities of the fluid on either side of the membrane, *R* is the radius of the cell membrane. Two-dimensional phospholipid bilayers have viscosities η_M <10^{-9} N s m^{-1} for temperatures above room T, and $\eta_{ext} \cong 10^{-3}$ Pa s, therefore η_{int} dominates the denominator of expression S.7, i.e. we are able to measure from this procedure the internal viscosity of the RBC. Finally, from $\tau_{\vec{q}}$, using the values of κ and σ obtained from the static spectrum of the same cell, we can then obtain the value of the internal viscosity of the RBC.

References:

1. Helfrich W, Servuss RM. Undulations, steric interaction and cohesion of fluid membranes. *Nuovo Cimento D*. 1984; 3:137.
2. Yoon YZ, Hong H, Brown A, *et al*. Flickering analysis of erythrocyte mechanical properties dependence on oxygenation level, cell shape, and hydration level. *Biophys J.* 2009;97(6):1606-1615.
3. Koch M, Wright KE, Otto O, *et al*. *Plasmodium falciparum* erythrocyte-binding antigen 175 triggers a biophysical change in the red blood cell that facilitates invasion. *Proc Natl Acad Sci USA.* 2017; 114(16):4225-4230.

4. Evans J, Gratzer W, Mohandas N, Parker K, Sleep J. Fluctuations of the red blood cell membrane: relation to mechanical properties and lack of ATP dependence. *Biophys J*. 94:4134-4144, 2008.
5. Yoon YZ, Kotar J, Brown AT, Cicuta P. Red blood cell dynamics: from spontaneous fluctuations to non-linear response. Soft Matter 2011; 7,2042.
6. Deserno M. Fluid lipid membranes - a primer. 2007. www.cmu.edu/biolphys/deserno/pdf/membrane theory.pdf.
7. Pecreaux J, Dobereiner HG, Prost J, Joanny JF, Bassereau P. Refined contour analysis of giant unilamellar vesicles. *Eur Phys J E Soft Matter.* 2004;13(3):277-290.
8. Betz T, Lenz M, Joanny JF, Sykes C. ATP-dependent mechanics of red blood cells. *Proc Natl Acad Sci USA.* 2009;106(36):15320–15325.
9. Hale JP, Marcelli G, Parker KH, Winlove CP, Petrov PG. Red blood cell thermal fluctuations: comparison between experiment and molecular dynamics simulations. *Soft Matter.* 2009;5(19):3603-3606.
10. Gov N, Zilman AG, Safran S. Cytoskeleton confinement and tension of red blood cell membranes. *Phys. Rev. Lett*. 2003;90(22):228101.
11. Park YK, Best CA, Auth T, Gov NS, Safran SA, Popescu G, Suresh S, Feld MS. Metabolic remodeling of the human red blood cell membrane. *Proc. Nat. Acad. Sci*. 2010;107(4):1289-1294.

Supplementary Tables

Supplementary Table 1 | Study participant genotypes at 6 malaria-protective polymorphisms

Sample	Dantu (rs186873296)	*HbS* (rs334)	Alpha thalassaemia	*G6PD* (rs1050828)	*ATP2B4* (rs1541255)	*CR1* (rs17047661)	*ABO* (rs8176719)
MSC1	GG	AA	Het	CC	AA	AG	DI
MSC2	AG	AA	Norm	CT	AA	AA	DD
MSC3	AA	AA	Norm	CC	AA	AG	DD
MSC4	GG	AA	Norm	TT	AG	AG	II
MSC5	AG	AA	Norm	CC	AA	AG	DD
MSC6	AA	AA	Norm	CC	AA	-	-
MSC7	GG	AA	Norm	-	-	-	-
MSC8	AG	AA	Norm	CC	AA	AG	DD
MSC9	AA	AA	Norm	CC	AA	GG	DI
MSC 10	GG	AA	Het	-	-	-	-
MSC 11	AG	AA	Het	CC	AA	AG	DD
MSC 12	AA	AA	Norm	TT	AA	-	-
MSC 13	GG	AA	Het	-	-	-	-
MSC 14	AG	AA	Het	TT	AA	GG	DI
MSC 15	AA	AA	Norm	CC	AA	GG	DI
MSC 16	GG	-	-	-	-	-	-
MSC 17	AG	AA	Het	CT	AA	AG	DI
MSC 18	AA	AA	Norm	CC	AA	AG	DD
KBC1	GG	AA	Norm	CC	AA	GG	DI
KBC2	AA	AA	Norm	CC	AA	GG	DI
KBC3	AG	AA	Norm	CC	AA	GG	DI
KBC4	GG	AA	Norm	CC	GG	AG	DD
KBC5	AA	AA	Norm	CC	GG	AG	DD
KBC6	AA	AA	Norm	CC	AA	GG	DD
KBC7	GG	AA	Norm	CC	AA	GG	DD
KBC 8	AG	AA	Norm	CC	AA	GG	DD
KBC 9	AG	AA	Norm	CC	AG	GG	DI
KBC 10	GG	AA	Norm	CC	AG	GG	DI
KBC 11	AA	AA	Norm	CC	AG	GG	DI
KBC 12	AG	AA	Norm	CC	AA	AG	DD
KBC 13	GG	AA	Norm	CC	AA	AG	DD
KBC 14	AA	AA	Norm	CC	AA	AG	DD
KBC 15	AG	AA	Norm	CC	AA	GG	DI

KBC 16	AA	AA	Norm	CC	AA	GG	II
KBC 17	GG	AA	Norm	CC	AA	GG	II
KBC 18	AA	AA	Norm	CC	AG	GG	DD
KBC 19	AG	AA	Norm	CC	AG	GG	DD
KBC 20	GG	AA	Norm	CC	AG	GG	DD
KBC 21	AA	AA	Norm	CC	AA	GG	DI
KBC 22	AG	AA	Norm	CC	GG	AG	DI
KBC 23	AA	AA	Norm	CC	GG	AG	DI
KBC 24	AG	AA	Norm	CC	AA	GG	II

Study participant genotype information for malaria-protective polymorphisms including Dantu (rs186873296), *HBB* (rs334), alpha-thalassaemia, *G6PD* (rs1050828), *ATP2B4* (rs1541255) and *CR1* (rs17047661), and *ABO* (rs8176719). Study subjects were obtained from two cohorts, from which both frozen and fresh red blood cell (RBC) samples were obtained. Genotypes were controlled within each experimental set of Dantu homozygous protective genotype (rs186873296=GG), heterozygote protective genotype (rs186873296=AG), and non-Dantu (rs186873296=AA) individuals.

The definition of all other genotypes is as follows:

HBB - rs334: **AA**-non-sickle; **AS**-sickle cell trait; **SS**-sickle cell disease

Alpha-thalassaemia: **Norm**-homozygous reference genotype; **Het**-heterozygous protective genotype; **Hom**-homozygous protective genotype

G6PD - rs1050828: **CC**-homozygous reference genotype; **CT**-heterozygous protective genotype; **TT**-homozygous protective genotype

ATP2B4 - rs1541255: **AA**-homozygous reference genotype; **AG**-heterozygous protective genotype; **GG**-homozygous protective genotype

CR1 - rs17047661: **GG**-homozygous reference genotype; **AG**-heterozygous protective genotype; **AA**-homozygous protective genotype

ABO - rs8176719: **DD**-blood group O; **DI** or **II**-blood group A, B or AB

Supplementary Table 2 | Preference invasion into Dantu variant RBCs

	one-way ANOVA across Dantu genotype groups	Pairwise comparisons of mean parasitaemia differences across Dantu genotype groups					
Parasite strain	**P value**	**non-Dantu-Dantu hom (%)**	**P adj**	**non-Dantu-Dantu het (%)**	**P adj**	**Dantu het-Dantu hom (%)**	**P adj**
3D7	0.001	2.1134 (0.9551 - 3.2718)	0.001 **	0.9569 (-0.2014 - 2.1153)	0.114	1.1565 (-0.0019 - 2.3149)	0.050
Dd2	0.018	2.7888 (0.535 - 5.0426)	0.015 *	1.012 (-1.2418 - 3.2658)	0.490	1.7768 (-0.477 - 4.0306)	0.135
SAO75	0.035	2.0798 (0.212 - 3.9476)	0.028 *	0.8854 (-0.9824 - 2.7532)	0.454	1.1945 (-0.6733 - 3.0623)	0.252
GB4	0.122	0.6852 (-1.6704 - 3.0408)	0.719	1.8461 (-0.3747 - 4.067)	0.107	1.1609 (-1.1947 - 3.5166)	0.961
7G8	0.212	0.9928 (-1.7233 - 3.7089)	0.619	1.9408 (-0.7753 - 4.6569)	0.186	0.948 (-1.7681 - 3.6641)	0.967
ΔPfEBA175	0.028	1.3932 (0.056 - 2.7303)	0.040 *	1.2441 (-0.093 - 2.5813)	0.072	0.1491 (-1.2146 - 1.5127)	0.408

Mean difference in parasitaemia between Dantu genotype groups (n=6 biologically independent samples per genotype group) is compared using the one-way ANOVA, and pairwise comparisons with p-values adjusted for multiple comparisons (P adj) using Tukey HSD test. The lower and upper limits of the differences in parasitaemia are given in parentheses. ** $p < 0.01$; * $p < 0.05$

Supplementary Table 3 | Merozoite-RBC adhesion force measured by optical tweezers

	Non-Dantu (Mean ± SD)	Dantu heterozygote (Mean ± SD)	Dantu homozygote (Mean ± SD)
Number of cells	19	21	24
Merozoite-erythrocyte attachment force	42.5 ± 15.7	49.5 ± 22.9	39.8 ± 15.6

Adhesive forces between merozoites and RBCs during invasion were measured using optical tweezers, as explained in detail in the Methods. Mean and standard deviation (SD) of data in **Supplementary Fig. 3** for the three genotype groups are shown.

Supplementary Table 4 | Proteomic data from plasma membrane profiling by tandem mass tag (TMT)-based MS3 mass spectrometry

Uniprot	Protein Name	Gene Symbol	Number of peptides	non-Dantu #1	non-Dantu #2	non-Dantu #3	Dantu het #1	Dantu het #2	Dantu het #3	Dantu hom #1	Dantu hom #2	Dantu hom #3	Fold Change Dantu Hom/non-Dantu	Significance A
Q86UD5	Mitochondrial sodium/hydrogen exchanger 9B2	SLC9B2	1	24	32	33	161	277	137	522	587	573	18.81	8.17E-11
P15529-2	Membrane cofactor protein	CD46	2	61	64	87	208	246	1176	401	580	1248	10.53	2.49E-07
Q9H015	Solute carrier family 22 member 4	SLC22A4	7	130	139	211	111	251	8007	135	1031	2769	8.20	4.62E-06
P02786	Transferrin receptor protein 1	CD71	21	1506	1772	1215	12127	4928	3092	10872	3846	14571	6.52	5.12E-05
O95980	Reversion-inducing cysteine-rich protein with Kazal motifs	RECK	5	290	383	278	541	431	477	815	3893	375	5.35	3.27E-04
P54709	Sodium/potassium-transporting ATPase subunit beta-3	ATP1B3	7	937	402	350	1004	2463	1130	3271	2886	2392	5.06	5.29E-04
Q01650	Large neutral amino acids transporter small subunit 1	SLC7A5	1	23	26	21	71	83	37	86	47	212	4.87	7.34E-04
Q9P0T7	Transmembrane protein 9	TMEM9	6	620	619	967	795	1039	692	5185	2588	2846	4.81	8.10E-04
Q03252	Lamin-B2	LMNB2	2	147	145	124	170	151	122	762	924	159	4.43	1.59E-03
P05026	Sodium/potassium-transporting ATPase subunit beta-1	ATP1B1	13	1257	1233	1089	6314	4911	3390	5396	3427	4592	3.75	5.56E-03
P48029	Sodium- and chloride-dependent creatine transporter 1	SLC6A8	8	291	440	415	222	309	2695	282	1115	2773	3.64	6.83E-03
P16671	Platelet glycoprotein 4	CD36	9	1315	1453	1177	1460	1676	2507	2954	5583	5366	3.52	8.56E-03
Q8WUY1	Protein THEM6	THEM6	2	114	146	108	289	222	169	476	358	456	3.51	8.83E-03
P14209	CD99 antigen	CD99	20	1402	2861	1462	917	4176	955	10207	4534	4667	3.39	1.11E-02
O14662	Syntaxin-16	STX16	1	172	99	110	81	96	90	123	136	1000	3.31	1.30E-02
Q9H8M5	Metal transporter CNNM2	CNNM2	4	289	279	278	323	288	392	747	845	963	3.02	2.30E-02
P06213	Insulin receptor	INSR	15	2239	1988	1773	3039	3840	4078	5552	7108	5261	2.99	2.46E-02
Q9HD45	Transmembrane 9 superfamily member 3	TM9SF3	3	98	132	143	101	230	83	303	496	276	2.88	3.04E-02
Q13444	Disintegrin and metalloproteinase domain-containing protein 15	ADAM15	1	23	25	38	31	325	36	47	157	37	2.83	3.36E-02
P05556	Integrin beta-1	ITGB1	7	918	937	900	1020	1072	4140	1465	2493	3781	2.81	3.52E-02
Q08174-2	Protocadherin-1	PCDH1	20	2608	1791	1979	1845	2586	2086	10384	4459	2946	2.79	3.67E-02

Q9Y289	Sodium-dependent multivitamin transporter	SLC5A6	1	36	37	40	23	38	251	39	95	164	2.65	4.83E-02
P08069	Insulin-like growth factor 1 receptor	IGF1R	8	826	728	803	1408	1487	1664	1664	2534	1749	2.52	6.33E-02
Q15758	Neutral amino acid transporter B(0)	SLC1A5	2	225	293	322	379	481	375	609	542	930	2.48	6.92E-02
P18433	Receptor-type tyrosine-protein phosphatase alpha	PTPRA	31	5021	5172	3199	6103	8167	5916	14135	11403	7259	2.45	7.36E-02
P31995	Low affinity immunoglobulin gamma Fc region receptor II-c	FCGR2C	1	142	63	126	108	102	134	432	218	135	2.38	8.57E-02
P54852	Epithelial membrane protein 3	EMP3	4	743	877	926	1153	1468	2069	1656	2038	2055	2.26	1.09E-01
P60903	Protein S100-A10	S100A10	3	725	584	118	419	132	72	1326	1681	112	2.19	1.27E-01
Q53GQ0	Estradiol 17-beta-dehydrogenase 12	HSD17B12	6	605	610	570	945	769	766	2061	1096	649	2.13	1.42E-01
P50895	Basal cell adhesion molecule	BCAM	112	9406	15885	18802	8882	23703	14094	31114	34364	26310	2.08	1.57E-01
Q9NQ34	Transmembrane protein 9B	TMEM9B	5	773	655	901	902	781	785	2310	1332	1193	2.08	1.59E-01
Q6UVK1	Chondroitin sulfate proteoglycan 4	CSPG4	1	23	36	30	23	42	25	47	53	79	2.02	1.79E-01
Q6PCB8	Embigin	EMB	2	95	203	327	324	401	133	293	323	636	2.00	1.85E-01
Q15517	Corneodesmosin	CDSN	2	781	752	634	1003	1046	1076	1503	1556	1267	2.00	1.87E-01
O60449-2	Lymphocyte antigen 75	LY75	4	296	315	310	401	765	546	590	567	633	1.94	2.10E-01
P08195-4	4F2 cell-surface antigen heavy chain	SLC3A2	17	3047	3358	3366	5085	4857	3912	6122	4825	7889	1.93	2.16E-01
Q7KYR7-1	Butyrophilin subfamily 2 member A1	BTN2A1	12	1617	789	1463	1821	2753	2003	2195	2229	2939	1.90	2.28E-01
P08575	Receptor-type tyrosine-protein phosphatase C	PTPRC	19	3042	2825	3022	3710	5428	6515	4608	6500	5763	1.90	2.30E-01
Q8WUX1	Sodium-coupled neutral amino acid transporter 5	SLC38A5	2	441	470	495	569	520	1181	531	736	1366	1.87	2.43E-01
P05023-4	Sodium/potassium-transporting ATPase subunit alpha-1	ATP1A1	43	8216	7522	6845	11353	12872	8631	12810	10757	18474	1.86	2.48E-01
P15151	Poliovirus receptor	PVR	4	478	389	891	813	1775	1353	1221	972	1039	1.84	2.60E-01
Q9UBI6	Guanine nucleotide-binding protein G(I)/G(S)/G(O) subunit gamma-12	GNG12	1	84	86	24	28	24	21	136	142	77	1.82	2.68E-01
Q7L1W4	Leucine-rich repeat-containing protein 8D	LRRC8D	1	23	23	18	22	32	35	40	47	30	1.81	2.78E-01
Q5T4S7-2	E3 ubiquitin-protein ligase UBR4	UBR4	135	20342	15621	14499	23262	42016	27041	37768	18978	33400	1.79	2.89E-01
Q8IWT6	Leucine-rich repeat-containing protein 8A	LRRC8A	3	198	193	167	201	281	330	284	446	265	1.79	2.90E-01
P17813	Endoglin	ENG	23	3966	4002	3131	5074	7249	6985	6155	7337	5919	1.75	3.12E-01
Q16563	Synaptophysin-like protein 1	SYPL1	17	5090	3049	2541	5057	7314	5720	4969	6561	7070	1.74	3.16E-01
P02724	Glycophorin-A (Shared)	GYPA Shared	439	57855	66296	60248	92359	71317	76464	112479	103046	105388	1.74	3.17E-01

Q2LD37	Uncharacterized protein KIAA1109	KIAA1109	1	11	16	23	18	22	18	21	27	39	1.73	3.24E-01
P55011	Solute carrier family 12 member 2	SLC12A2	9	1862	1571	1669	3437	3592	2632	2043	3170	3613	1.73	3.24E-01
P61106	Ras-related protein Rab-14	RAB14	4	424	571	554	903	538	532	850	730	1074	1.71	3.36E-01
Q12913	Receptor-type tyrosine-protein phosphatase eta	PTPRJ	6	1231	1121	1044	1382	1823	1673	1723	2310	1748	1.70	3.43E-01
Q7Z4F1	Low-density lipoprotein receptor-related protein 10	LRP10	8	812	749	670	667	943	821	1738	1137	879	1.68	3.57E-01
P08473	Neprilysin	MME	2	190	195	122	162	217	167	317	330	200	1.67	3.64E-01
P08174-7	Complement decay-accelerating factor	CD55	122	21540	18780	18345	34764	20358	24121	35657	35584	24655	1.63	3.92E-01
O60888-2	Protein CutA	CUTA	1	22	24	29	40	34	36	35	49	38	1.63	3.99E-01
Q9UP95-7	Solute carrier family 12 member 4	SLC12A4	2	282	264	359	560	466	427	557	460	451	1.62	4.02E-01
Q9UHW9-2	Solute carrier family 12 member 6	SLC12A6	2	510	376	366	741	430	797	687	792	536	1.61	4.12E-01
P78410	Butyrophilin subfamily 3 member A2	BTN3A2	5	519	653	693	983	1051	609	1322	900	762	1.60	4.21E-01
Q12767-2	Uncharacterized protein KIAA0195	KIAA0195	8	669	727	787	1267	1513	1178	1119	982	1384	1.60	4.23E-01
P15144	Aminopeptidase N	ANPEP	4	537	484	191	253	194	180	684	1023	214	1.59	4.32E-01
Q9H0X4	Protein ITFG3	ITFG3	8	1724	846	1353	1052	2737	2512	2271	2054	1880	1.58	4.36E-01
P16070	CD44 antigen	CD44	111	22570	25060	25182	20499	43940	41766	39269	29641	45652	1.57	4.43E-01
Q99497	Protein DJ-1	PARK7	15	2133	3143	1941	5266	2859	2818	4700	2677	3907	1.56	4.52E-01
Q16610-4	Extracellular matrix protein 1	ECM1	1	145	128	132	86	209	165	125	210	296	1.56	4.56E-01
P14415	Sodium/potassium-transporting ATPase subunit beta-2	ATP1B2	12	2877	1630	1835	1984	2937	1974	2849	2804	4083	1.54	4.78E-01
O60486	Plexin-C1	PLXNC1	17	2926	2726	3563	3626	3379	4185	3371	4097	6294	1.49	5.18E-01
Q8TF66-2	Leucine-rich repeat-containing protein 15	LRRC15	1	16	26	53	22	24	22	28	40	72	1.49	5.22E-01
Q9BTV4	Transmembrane protein 43	TMEM43	1	212	167	24	44	48	27	232	309	55	1.48	5.33E-01
Q96PL5	Erythroid membrane-associated protein	ERMAP	39	8900	7660	7148	10478	9745	9720	13093	13241	8658	1.48	5.36E-01
P11279	Lysosome-associated membrane glycoprotein 1	LAMP1	5	275	276	283	929	652	728	217	509	503	1.47	5.38E-01
P11215-2	Integrin alpha-M	ITGAM	2	68	109	202	281	134	86	87	62	407	1.46	5.47E-01
Q96FZ7	Charged multivesicular body protein 6	CHMP6	1	268	309	224	340	273	289	371	433	352	1.44	5.70E-01
Q9H0U4	Ras-related protein Rab-1B	RAB1B	1	188	155	130	202	274	195	253	246	182	1.44	5.73E-01
P20340-2	Ras-related protein Rab-6A	RAB6A	1	72	51	34	86	84	45	69	80	76	1.44	5.73E-01

O75396	Vesicle-trafficking protein SEC22b	SEC22B	2	186	179	136	246	181	170	264	271	181	1.43	5.86E-01
P22303-2	Acetylcholinesterase	ACHE	84	16474	15624	12835	21679	15077	9986	20244	24751	18510	1.41	6.04E-01
Q8WW22-2	DnaJ homolog subfamily A member 4	DNAJA4	5	1515	2124	1380	1865	2266	1420	2884	1846	2341	1.41	6.09E-01
Q02161	Blood group Rh(D) polypeptide	RHD	21	3324	3766	3498	5174	3384	3471	6909	4159	3743	1.40	6.20E-01
Q4KMQ2-2	Anoctamin-6	ANO6	6	1439	2250	1578	2733	1887	2476	2696	1425	3219	1.39	6.26E-01
O15440	Multidrug resistance-associated protein 5	ABCC5	34	7485	6139	8245	10919	10086	10682	9943	11532	8950	1.39	6.29E-01
Q5HYA8	Meckelin	TMEM67	1	69	66	82	74	120	97	33	134	134	1.38	6.38E-01
P61026	Ras-related protein Rab-10	RAB10	4	1072	959	541	1052	1325	998	1321	1221	1017	1.38	6.38E-01
Q9NZM1	Myoferlin	MYOF	2	371	392	161	146	189	176	538	552	185	1.38	6.43E-01
P02814	Submaxillary gland androgen-regulated protein 3B	SMR3B	1	25	30	33	25	29	33	47	42	32	1.37	6.54E-01
Q15907	Ras-related protein Rab-11B	RAB11B	1	192	126	58	120	131	77	127	255	133	1.37	6.56E-01
Q96Q45-3	Transmembrane protein 237	TMEM237	6	1266	1742	1748	1811	1720	2288	1815	2383	2291	1.36	6.61E-01
P05107	Integrin beta-2	ITGB2	3	92	131	363	497	257	196	99	114	586	1.36	6.62E-01
Q92692	Poliovirus receptor-related protein 2	PVRL2	3	281	146	315	238	566	512	322	395	288	1.35	6.73E-01
P16615	Sarcoplasmic/endoplasmic reticulum calcium ATPase 2	ATP2A2	2	87	116	80	84	89	61	159	133	90	1.35	6.82E-01
Q04941	Proteolipid protein 2	PLP2	3	605	826	593	814	721	1241	484	990	1253	1.35	6.82E-01
Q9NRQ2	Phospholipid scramblase 4	PLSCR4	4	587	350	407	417	703	724	499	866	448	1.35	6.83E-01
Q9UHW9	Solute carrier family 12 member 6	SLC12A6	23	5935	4140	4275	6608	7453	10089	5822	8315	5163	1.34	6.86E-01
Q9Y639	Neuroplastin	NPTN	23	4308	5760	5406	6457	6833	5113	6512	7458	6795	1.34	6.90E-01
Q9UIQ6	Leucyl-cystinyl aminopeptidase	LNPEP	6	841	656	659	832	848	924	876	1373	634	1.34	6.95E-01
P54760	Ephrin type-B receptor 4	EPHB4	22	3025	3509	3705	4611	4751	4890	3322	5432	4929	1.34	6.96E-01
O94919	Endonuclease domain-containing 1 protein	ENDOD1	14	1703	2178	1302	3105	2182	1908	3046	1955	1882	1.33	7.07E-01
Q9Y6R1-5	Electrogenic sodium bicarbonate cotransporter 1	SLC4A4	2	94	81	75	120	137	148	116	112	103	1.33	7.11E-01
Q04656-3	Copper-transporting ATPase 1	ATP7A	67	13630	12557	11899	21504	18302	18286	17476	15029	17887	1.32	7.14E-01
Q13443	Disintegrin and metalloproteinase domain-containing protein 9	ADAM9	5	594	670	710	791	760	662	1006	648	954	1.32	7.16E-01
O00161	Synaptosomal-associated protein 23	SNAP23	2	92	102	107	123	137	127	131	111	155	1.32	7.18E-01
Q8ND76	Cyclin-Y	CCNY	2	72	87	81	94	113	131	97	106	112	1.31	7.34E-01

P51811	Membrane transport protein XK	XK	38	6724	7473	7533	9218	8101	8325	9530	8113	10695	1.30	7.39E-01
Q92542	Nicastrin	NCSTN	16	2643	2986	3368	3622	3536	3992	3852	3358	4501	1.30	7.42E-01
Q9Y666	Solute carrier family 12 member 7	SLC12A7	33	5572	4922	6781	7408	10318	7599	6956	8022	7441	1.30	7.47E-01
A2RU67	Uncharacterized protein KIAA1467	KIAA1467	2	231	260	275	325	189	250	485	296	210	1.29	7.55E-01
Q8N370-3	Large neutral amino acids transporter small subunit 4	SLC43A2	44	13969	8839	10092	13307	15015	13408	13226	20231	8611	1.28	7.73E-01
P19256	Lymphocyte function-associated antigen 3	CD58	45	11514	9683	14983	20833	11869	11771	17879	13145	15077	1.27	7.79E-01
O15498	Synaptobrevin homolog YKT6	YKT6	1	77	63	39	82	68	43	61	55	109	1.26	7.97E-01
Q14254	Flotillin-2	FLOT2	8	2256	2263	1531	4789	1532	2097	2717	2894	1996	1.26	8.03E-01
Q93070	Ecto-ADP-ribosyltransferase 4	ART4	26	8340	6735	5675	10540	8957	6267	9466	8423	8128	1.25	8.08E-01
P78310	Coxsackievirus and adenovirus receptor	CXADR	14	3167	2651	2800	2861	3033	3147	3160	4164	3460	1.25	8.12E-01
P51790	H(+)/Cl(-) exchange transporter 3	CLCN3	14	2596	2727	2936	4867	2256	2623	4942	3341	2050	1.25	8.12E-01
Q9UIW2	Plexin-A1	PLXNA1	40	5316	7287	6218	9013	9172	11923	6305	9095	7990	1.24	8.24E-01
P08637	Low affinity immunoglobulin gamma Fc region receptor III-A	FCGR3A	1	62	40	242	243	99	58	231	84	112	1.24	8.32E-01
P28907	ADP-ribosyl cyclase 1	CD38	17	899	6389	8367	1925	4947	964	5446	6080	7831	1.24	8.33E-01
P01112	GTPase HRas	HRAS	2	656	517	462	696	659	679	637	765	594	1.22	8.55E-01
Q6P1A2	Lysophospholipid acyltransferase 5	LPCAT3	1	67	66	60	89	70	55	82	80	72	1.21	8.66E-01
Q9HCJ1	Progressive ankylosis protein homolog	ANKH	3	472	364	445	534	408	299	677	397	481	1.21	8.67E-01
Q9Y6M5	Zinc transporter 1	SLC30A1	49	11985	10554	13211	16054	17334	14415	11328	18387	13113	1.20	8.91E-01
Q07065	Cytoskeleton-associated protein 4	CKAP4	7	1460	1427	252	232	388	229	1166	2029	563	1.20	8.92E-01
P23284	Peptidyl-prolyl cis-trans isomerase B	PPIB	1	109	71	7	22	14	5	56	154	12	1.19	8.98E-01
P48067	Sodium- and chloride-dependent glycine transporter 1	SLC6A9	2	254	268	253	224	264	448	287	283	353	1.19	9.03E-01
P50416	Carnitine O-palmitoyltransferase 1, liver isoform	CPT1A	2	264	308	301	337	297	328	468	295	276	1.19	9.04E-01
Q9H3N1	Thioredoxin-related transmembrane protein 1	TMX1	1	47	51	45	46	51	51	54	68	46	1.18	9.14E-01
Q02094	Ammonium transporter Rh type A	RHAG	52	7462	7216	8759	8337	8531	9951	8189	10224	9255	1.18	9.18E-01
Q9NP72-2	Ras-related protein Rab-18	RAB18	1	194	327	199	426	204	245	249	379	220	1.18	9.22E-01
P98172	Ephrin-B1	EFNB1	18	3299	3407	4038	4919	3695	3650	4250	3792	4600	1.18	9.23E-01
P04921	Glycophorin-C	GYPC	206	33328	32546	28576	34062	29295	30269	37566	41837	31371	1.17	9.29E-01

P00387-3	NADH-cytochrome b5 reductase 3	CYB5R3	3	148	130	77	97	75	71	147	175	94	1.17	9.30E-01
Q92482	Aquaporin-3	AQP3	5	1214	1362	1252	1730	1247	1326	1220	1633	1635	1.17	9.30E-01
P84085	ADP-ribosylation factor 5	ARF5	2	286	343	185	619	411	173	436	259	258	1.17	9.33E-01
P98196	Probable phospholipid-transporting ATPase IH	ATP11A	4	284	344	367	496	372	397	379	333	444	1.16	9.47E-01
P09601	Heme oxygenase 1	HMOX1	1	79	99	58	43	91	56	72	115	87	1.16	9.47E-01
Q9UMF0	Intercellular adhesion molecule 5	ICAM5	3	369	506	360	312	383	696	518	455	458	1.16	9.51E-01
Q93050-3	V-type proton ATPase 116 kDa subunit a isoform 1	ATP6V0A1	8	1228	1011	1314	1223	1204	1339	1259	1374	1483	1.16	9.52E-01
Q13261	Interleukin-15 receptor subunit alpha	IL15RA	8	1668	1747	1743	1796	2344	1052	3173	1445	1354	1.16	9.53E-01
B2RUZ4	Small integral membrane protein 1	SMIM1	5	947	678	338	844	440	802	958	946	356	1.15	9.62E-01
Q9Y5Z0	Beta-secretase 2	BACE2	5	328	1005	645	513	630	733	686	694	891	1.15	9.68E-01
P33527	Multidrug resistance-associated protein 1	ABCC1	83	14571	14871	12565	13896	10360	19221	15126	18842	14216	1.15	9.70E-01
P62191	26S protease regulatory subunit 4	PSMC1	7	1144	1645	1201	1965	1532	1405	1359	1295	1917	1.15	9.73E-01
Q8IUW5	RELT-like protein 1	RELL1	12	1658	1400	1616	1756	1932	2024	1565	1922	1855	1.14	9.77E-01
O75326	Semaphorin-7A	SEMA7A	57	14034	8984	11617	16262	10123	11963	11424	15287	12712	1.14	9.85E-01
Q10589	Bone marrow stromal antigen 2	BST2	11	1848	1414	2047	2804	2925	2196	1986	2236	1819	1.14	9.86E-01
P49768	Presenilin-1	PSEN1	1	62	65	57	70	61	55	83	54	71	1.13	9.93E-01
P35613	Basigin	BSG	84	18356	21573	19196	21771	24115	25996	24897	22360	19720	1.13	9.93E-01
Q9NV96	Cell cycle control protein 50A	TMEM30A	20	4323	4077	4724	5205	5214	5620	4136	5382	5307	1.13	9.98E-01
P13073	Cytochrome c oxidase subunit 4 isoform 1, mitochondrial	COX4I1	2	588	516	97	89	102	77	495	751	110	1.13	1.00E+00
Q8IZY2	ATP-binding cassette sub-family A member 7	ABCA7	42	9017	8325	7040	9440	7642	10578	5543	7783	14189	1.13	1.00E+00
P35670	Copper-transporting ATPase 2	ATP7B	1	101	133	132	138	76	88	113	151	147	1.13	9.95E-01
Q92859	Neogenin	NEO1	2	40	65	70	67	58	75	72	62	63	1.12	9.92E-01
P23276	Kell blood group glycoprotein	KEL	132	22381	25093	26922	26374	22382	24615	29400	26065	27693	1.12	9.82E-01
Q9NUQ9	Protein FAM49B	FAM49B	1	49	48	30	49	46	52	63	37	41	1.11	9.65E-01
Q9P035	Very-long-chain (3R)-3-hydroxyacyl-[acyl-carrier protein] dehydratase 3	PTPLAD1	1	46	42	26	38	28	31	51	48	25	1.10	9.49E-01
Q9Y5S1	Transient receptor potential cation channel subfamily V member 2	TRPV2	4	653	643	707	518	823	818	599	801	798	1.10	9.48E-01
Q92485	Acid sphingomyelinase-like phosphodiesterase 3b	SMPDL3B	5	1131	760	1086	1018	1132	1143	1065	1172	1026	1.10	9.45E-01

Q96BI3	Gamma-secretase subunit APH-1A	APH1A	2	276	425	363	529	314	429	334	408	424	1.10	9.45E-01
Q8WUD1	Ras-related protein Rab-2B	RAB2B	1	101	150	146	122	150	103	103	101	230	1.09	9.42E-01
O15439	Multidrug resistance-associated protein 4	ABCC4	161	35175	31325	38485	34277	36989	43698	40399	32901	40478	1.08	9.24E-01
P62241	40S ribosomal protein S8	RPS8	1	196	241	45	97	56	19	154	282	84	1.08	9.10E-01
P05186	Alkaline phosphatase, tissue-nonspecific isozyme	ALPL	3	250	95	107	230	177	149	237	113	137	1.08	9.09E-01
P61006	Ras-related protein Rab-8A	RAB8A	5	3472	3476	2454	3098	2922	3276	3076	3650	3353	1.07	9.03E-01
Q9UNQ0	ATP-binding cassette sub-family G member 2	ABCG2	22	5689	4886	6034	6057	6954	6041	5445	6920	5431	1.07	9.03E-01
P23634-2	Plasma membrane calcium-transporting ATPase 4	ATP2B4	1	122	167	100	159	149	165	99	169	145	1.06	8.88E-01
Q5T3F8	Transmembrane protein 63B	TMEM63B	20	4639	3342	4255	5712	2960	4425	6461	3266	3262	1.06	8.85E-01
Q8NB49	Probable phospholipid-transporting ATPase IG	ATP11C	8	1711	1981	2363	2333	2582	2504	1672	2000	2739	1.06	8.80E-01
P61225	Ras-related protein Rap-2b	RAP2B	9	1178	2028	2140	2299	1400	1921	1642	1690	2317	1.06	8.76E-01
P49913	Cathelicidin antimicrobial peptide	CAMP	4	173	312	1940	1826	714	387	99	223	2237	1.06	8.75E-01
O75695	Protein XRP2	RP2	3	325	379	301	403	359	334	297	358	403	1.05	8.71E-01
P20339	Ras-related protein Rab-5A	RAB5A	4	205	231	218	293	273	201	179	226	283	1.05	8.71E-01
P21439-2	Multidrug resistance protein 3	ABCB4	3	160	141	252	85	326	255	92	277	213	1.05	8.70E-01
P08962	CD63 antigen	CD63	1	10	21	54	81	25	26	6	9	73	1.05	8.62E-01
P16150	Leukosialin	SPN	1	48	54	68	31	55	137	47	50	81	1.05	8.60E-01
Q9Y2G3	Probable phospholipid-transporting ATPase IF	ATP11B	10	1300	1139	1367	1249	1888	1416	982	1352	1633	1.04	8.51E-01
Q15836	Vesicle-associated membrane protein 3	VAMP3	3	306	217	202	213	195	324	297	266	189	1.04	8.43E-01
Q9NTJ5	Phosphatidylinositide phosphatase SAC1	SACM1L	7	1092	1170	951	1318	879	828	1623	961	734	1.03	8.36E-01
O60884	DnaJ homolog subfamily A member 2	DNAJA2	3	671	1028	684	1101	621	478	1207	540	701	1.03	8.25E-01
P18085	ADP-ribosylation factor 4	ARF4	1	77	63	41	79	80	36	53	64	68	1.03	8.23E-01
P08754	Guanine nucleotide-binding protein G(k) subunit alpha	GNAI3	4	743	824	597	828	865	656	706	690	821	1.02	8.20E-01
A1A5C7	Solute carrier family 22 member 23	SLC22A23	26	5784	7746	5948	8519	7355	9764	4631	7545	7757	1.02	8.18E-01
Q8NHG7	Small VCP/p97-interacting protein	SVIP	2	642	388	368	391	479	558	373	527	527	1.02	8.14E-01
P51795-2	H(+)/Cl(-) exchange transporter 5	CLCN5	1	40	35	32	54	35	37	35	48	25	1.02	8.10E-01
Q14773	Intercellular adhesion molecule 4	ICAM4	67	17849	13730	16311	12510	8205	15983	15383	19049	14028	1.01	7.97E-01

Q92956	Tumor necrosis factor receptor superfamily member 14	TNFRSF14	6	1327	1232	1072	1288	1315	1673	1161	1382	1095	1.00	7.79E-01
Q15904	V-type proton ATPase subunit S1	ATP6AP1	5	561	353	454	383	427	437	385	587	395	1.00	7.75E-01
O15431	High affinity copper uptake protein 1	SLC31A1	6	1665	2053	1422	2712	1610	2073	1529	1866	1733	1.00	7.72E-01
P35813-3	Protein phosphatase 1A	PPM1A	5	541	786	678	968	677	648	646	690	664	1.00	7.70E-01
P22694-2	cAMP-dependent protein kinase catalytic subunit beta	PRKACB	2	419	377	248	539	386	505	415	253	369	0.99	7.65E-01
Q92508	Piezo-type mechanosensitive ion channel component 1	PIEZO1	87	12035	13875	11568	12062	18105	16664	11527	13112	12565	0.99	7.62E-01
P25686	DnaJ homolog subfamily B member 2	DNAJB2	10	2120	2470	1536	2470	1980	2546	2823	1584	1666	0.99	7.60E-01
P51793	H(+)/Cl(-) exchange transporter 4	CLCN4	4	591	471	546	578	569	584	496	701	381	0.98	7.40E-01
P23634	Plasma membrane calcium-transporting ATPase 4	ATP2B4	37	6391	9256	6145	8346	8764	7445	6069	7395	7885	0.98	7.39E-01
O15162	Phospholipid scramblase 1	PLSCR1	5	936	697	840	1095	1288	1095	582	1182	656	0.98	7.38E-01
Q9NY35	Claudin domain-containing protein 1	CLDND1	2	188	253	343	290	283	380	187	268	310	0.98	7.31E-01
Q08722	Leukocyte surface antigen CD47	CD47	71	18272	15457	15715	14511	15596	14353	14432	19632	14094	0.97	7.29E-01
Q5VW32	BRO1 domain-containing protein BROX	BROX	1	180	206	120	222	147	149	143	219	125	0.96	7.06E-01
P04843	Dolichyl-diphosphooligosaccharide--protein glycosyltransferase subunit 1	RPN1	2	1129	1001	470	282	354	361	772	1331	378	0.95	6.93E-01
Q969E2	Secretory carrier-associated membrane protein 4	SCAMP4	1	67	62	53	60	70	53	64	63	47	0.95	6.84E-01
P63218	Guanine nucleotide-binding protein G(I)/G(S)/G(O) subunit gamma-5	GNG5	1	467	425	236	412	418	396	315	411	343	0.95	6.81E-01
P13987	CD59 glycoprotein	CD59	58	14079	11466	15241	13358	11255	13600	11836	16193	10621	0.95	6.81E-01
P43007	Neutral amino acid transporter A	SLC1A4	1	59	116	107	131	106	118	78	62	126	0.94	6.70E-01
Q9NP58	ATP-binding cassette sub-family B member 6, mitochondrial	ABCB6	79	12902	11947	8541	13107	14168	13236	11089	10845	9367	0.94	6.62E-01
P17927	Complement receptor type 1	CR1	81	19506	14424	18073	11199	15036	13132	15517	13556	19447	0.93	6.54E-01
Q13336-2	Urea transporter 1	SLC14A1	52	11856	10329	10650	12486	9340	14119	10712	9134	10625	0.93	6.45E-01
O60488	Long-chain-fatty-acid--CoA ligase 4	ACSL4	2	184	239	197	216	202	201	188	220	166	0.93	6.42E-01
P41440	Folate transporter 1	SLC19A1	6	913	852	1856	1257	1487	1219	1152	831	1371	0.93	6.42E-01
Q15109-6	Advanced glycosylation end product-specific receptor	AGER	3	135	359	260	308	218	245	244	204	244	0.92	6.27E-01
Q8TDB8-5	Solute carrier family 2, facilitated glucose transporter member 14	SLC2A14	30	5829	5935	6942	5179	5960	4798	5801	5024	6148	0.91	6.08E-01
P60953	Cell division control protein 42 homolog	CDC42	4	1121	1223	1385	1303	1145	1220	966	1137	1273	0.91	6.04E-01

Q13308-6	Inactive tyrosine-protein kinase 7	PTK7	6	448	543	390	432	536	388	501	349	394	0.90	5.96E-01
Q5VY43	Platelet endothelial aggregation receptor 1	PEAR1	13	1878	2510	1849	1216	2711	1738	2234	1551	1832	0.90	5.95E-01
Q9Y624	Junctional adhesion molecule A	F11R	44	11988	10403	11173	12369	8948	7262	8211	10390	11623	0.90	5.95E-01
Q00013	55 kDa erythrocyte membrane protein	MPP1	30	9565	9495	8490	10239	8962	9648	7632	8436	8706	0.90	5.93E-01
P20020	Plasma membrane calcium-transporting ATPase 1	ATP2B1	26	5408	7240	5906	5647	6779	7122	4242	6585	5757	0.89	5.83E-01
Q7Z3C6	Autophagy-related protein 9A	ATG9A	1	73	204	76	300	69	125	163	106	43	0.88	5.66E-01
O95562	Vesicle transport protein SFT2B	SFT2D2	2	301	344	283	225	267	283	328	251	238	0.88	5.60E-01
P29972	Aquaporin-1	AQP1	19	3732	3350	3734	3236	4665	2848	2491	3847	3186	0.88	5.59E-01
P11166	Solute carrier family 2, facilitated glucose transporter member 1	SLC2A1	361	87788	99221	92544	100919	85546	89671	79632	84632	81305	0.88	5.55E-01
P04899-4	Guanine nucleotide-binding protein G(i) subunit alpha-2	GNAI2	2	107	103	100	109	115	117	61	94	115	0.87	5.47E-01
Q86T03-2	Type 1 phosphatidylinositol 4,5-bisphosphate 4-phosphatase	TMEM55B	1	33	21	18	25	23	32	14	29	20	0.87	5.45E-01
Q08357	Sodium-dependent phosphate transporter 2	SLC20A2	1	127	174	164	154	138	138	158	110	133	0.86	5.26E-01
Q96D31	Calcium release-activated calcium channel protein 1	ORAI1	4	1092	1253	652	1331	1072	1616	504	1060	1014	0.86	5.23E-01
P14207	Folate receptor beta	FOLR2	3	769	795	882	631	618	535	766	845	471	0.85	5.06E-01
Q5FWE3	Proline-rich transmembrane protein 3	PRRT3	2	155	174	165	135	143	160	125	171	113	0.83	4.71E-01
Q92581-2	Sodium/hydrogen exchanger 6	SLC9A6	7	1410	1355	1191	1354	1115	1432	1220	1151	902	0.83	4.65E-01
Q99828-2	Calcium and integrin-binding protein 1	CIB1	2	188	101	150	143	145	149	110	113	140	0.83	4.61E-01
Q9BX97	Plasmalemma vesicle-associated protein	PLVAP	12	3754	1508	2719	2031	3921	5514	1895	1541	3120	0.82	4.54E-01
O60931-2	Cystinosin	CTNS	2	163	286	191	165	177	145	130	152	242	0.82	4.49E-01
Q8IU68	Transmembrane channel-like protein 8	TMC8	8	3097	1189	2353	2027	1464	2425	1529	1673	2220	0.82	4.46E-01
P16452-2	Erythrocyte membrane protein band 4.2	EPB42	76	13112	14488	19292	15130	16042	14301	10599	11054	16521	0.81	4.42E-01
Q9H8H3	Methyltransferase-like protein 7A	METTL7A	2	143	68	71	108	112	112	88	80	62	0.81	4.41E-01
P32942	Intercellular adhesion molecule 3	ICAM3	13	3475	1237	1850	2058	2496	4787	1048	1774	2514	0.81	4.40E-01
P29966	Myristoylated alanine-rich C-kinase substrate	MARCKS	2	317	339	95	491	55	54	263	288	59	0.81	4.40E-01
O15400	Syntaxin-7	STX7	1	507	501	489	559	358	408	364	545	305	0.81	4.35E-01
P27105	Erythrocyte band 7 integral membrane protein	STOM	62	13702	14169	9583	10880	7715	24912	5122	12432	12758	0.81	4.34E-01
Q96DD7	Protein shisa-4	SHISA4	1	106	65	54	199	54	68	43	67	71	0.80	4.22E-01

P30825	High affinity cationic amino acid transporter 1	SLC7A1	6	1036	1706	2707	1032	1435	1146	1854	711	1755	0.79	4.06E-01
Q12907	Vesicular integral-membrane protein VIP36	LMAN2	6	975	1153	3269	907	1521	1392	1657	1499	1099	0.79	3.98E-01
Q8WWI5	Choline transporter-like protein 1	SLC44A1	4	1228	1381	1245	784	1080	1312	794	1123	1110	0.79	3.94E-01
O15554	Intermediate conductance calcium-activated potassium channel protein 4	KCNN4	14	4476	4325	3807	3477	4454	3440	2693	3024	4118	0.78	3.85E-01
O95297	Myelin protein zero-like protein 1	MPZL1	6	1850	1074	1977	1680	1412	1314	1112	1375	1274	0.77	3.64E-01
P51148-2	Ras-related protein Rab-5C	RAB5C	5	571	461	513	567	551	519	358	357	452	0.76	3.45E-01
O14828	Secretory carrier-associated membrane protein 3	SCAMP3	2	433	344	306	410	324	451	231	295	288	0.75	3.38E-01
P11169	Solute carrier family 2, facilitated glucose transporter member 3	SLC2A3	7	561	1451	565	1641	599	648	656	668	592	0.74	3.26E-01
Q7Z403	Transmembrane channel-like protein 6	TMC6	7	2021	610	1424	1114	880	1395	742	992	1277	0.74	3.25E-01
P04156	Major prion protein	PRNP	11	2225	2768	2187	2389	2274	3815	2380	1098	1854	0.74	3.25E-01
Q12846	Syntaxin-4	STX4	1	116	128	106	84	80	79	101	93	66	0.74	3.23E-01
A6NFX1	Major facilitator superfamily domain-containing protein 2B	MFSD2B	5	1614	1620	1202	1056	1330	1411	1051	1240	982	0.74	3.17E-01
O00461	Golgi integral membrane protein 4	GOLIM4	2	800	286	318	173	91	150	321	486	228	0.74	3.15E-01
Q6DD88	Atlastin-3	ATL3	1	535	290	27	65	32	249	253	357	18	0.74	3.15E-01
Q8N4S9	MARVEL domain-containing protein 2	MARVELD2	3	296	317	263	262	281	311	142	207	293	0.73	3.07E-01
Q68DH5	LMBR1 domain-containing protein 2	LMBRD2	1	395	356	455	287	254	305	319	354	201	0.72	2.96E-01
O15455	Toll-like receptor 3	TLR3	1	178	176	108	180	118	271	104	90	140	0.72	2.95E-01
Q53TN4	Cytochrome b reductase 1	CYBRD1	3	558	440	349	278	391	418	287	349	305	0.70	2.59E-01
P28906	Hematopoietic progenitor cell antigen CD34	CD34	4	1275	561	511	647	1451	2121	343	676	599	0.69	2.45E-01
P25942	Tumor necrosis factor receptor superfamily member 5	CD40	1	162	169	157	98	177	252	50	168	117	0.69	2.41E-01
Q9UL25	Ras-related protein Rab-21	RAB21	1	34	31	33	27	30	24	17	19	31	0.68	2.35E-01
Q9NP59	Solute carrier family 40 member 1	SLC40A1	96	26172	30560	31029	13472	20240	23717	23691	18301	17590	0.68	2.32E-01
P13598	Intercellular adhesion molecule 2	ICAM2	2	668	560	971	604	672	751	446	565	476	0.68	2.28E-01
P43250-2	G protein-coupled receptor kinase 6	GRK6	2	102	120	83	105	116	99	79	56	70	0.67	2.23E-01
P61020	Ras-related protein Rab-5B	RAB5B	1	1194	808	766	1027	967	795	567	673	543	0.64	1.87E-01
O95197	Reticulon-3	RTN3	1	184	205	191	110	91	83	106	181	85	0.64	1.82E-01
Q9H4G4	Golgi-associated plant pathogenesis-related protein 1	GLIPR2	4	715	750	495	552	455	467	448	317	482	0.64	1.77E-01

O00421-2	C-C chemokine receptor-like 2	CCRL2	10	1772	1586	1422	615	1246	1455	981	1275	767	0.63	1.72E-01
Q99808-2	Equilibrative nucleoside transporter 1	SLC29A1	69	16871	17545	18663	17824	15297	13370	11396	9321	12691	0.63	1.69E-01
P47900	P2Y purinoceptor 1	P2RY1	5	295	569	461	398	384	302	330	269	231	0.63	1.66E-01
Q9BTU6	Phosphatidylinositol 4-kinase type 2-alpha	PI4K2A	4	528	292	299	429	321	394	223	234	233	0.62	1.55E-01
Q6ZWT7	Lysophospholipid acyltransferase 2	MBOAT2	2	335	519	481	351	281	277	278	270	273	0.62	1.54E-01
P25445	Tumor necrosis factor receptor superfamily member 6	FAS	26	14653	8510	14592	6481	13991	10380	7894	8620	6577	0.61	1.49E-01
P63000-2	Ras-related C3 botulinum toxin substrate 1	RAC1	19	5280	5084	5275	4550	3786	3970	2540	3297	3461	0.59	1.31E-01
Q13530	Serine incorporator 3	SERINC3	13	2816	2498	2387	2842	1761	2328	2184	882	1408	0.58	1.18E-01
P62834	Ras-related protein Rap-1A	RAP1A	9	1852	1963	1881	1662	1815	1758	989	1189	974	0.55	9.35E-02
Q15223	Poliovirus receptor-related protein 1	PVRL1	28	5288	6530	6731	5852	5162	3964	3395	2946	3882	0.55	9.16E-02
Q8N9N7	Leucine-rich repeat-containing protein 57	LRRC57	10	2208	1574	1716	1297	2226	1793	706	788	1364	0.52	6.81E-02
P02730	Band 3 anion transport protein	SLC4A1	693	223434	192767	205221	137824	153679	134012	95150	100584	108756	0.49	4.96E-02
O14523-2	C2 domain-containing protein 2-like	C2CD2L	1	330	561	609	272	279	257	262	229	202	0.46	3.57E-02
P09543	2',3'-cyclic-nucleotide 3'-phosphodiesterase	CNP	15	2859	3125	3124	2506	3178	2482	1348	1030	1682	0.45	2.88E-02
P27701	CD82 antigen	CD82	10	1534	2505	2393	1412	936	1899	552	835	1465	0.44	2.79E-02
Q8IWA5	Choline transporter-like protein 2	SLC44A2	19	3058	4574	4429	2080	2019	3525	1050	1865	2380	0.44	2.63E-02
P32248	C-C chemokine receptor type 7	CCR7	3	1219	1715	767	349	785	551	621	479	506	0.43	2.45E-02
P11049	Leukocyte antigen CD37	CD37	1	65	143	31	33	63	48	28	39	37	0.43	2.45E-02
Q969X1	Protein lifeguard 3	TMBIM1	3	360	487	321	218	218	308	165	178	157	0.43	2.26E-02
Q96HA4	Uncharacterized protein C1orf159	C1orf159	2	668	797	960	446	524	503	287	385	318	0.41	1.67E-02
P53985	Monocarboxylate transporter 1	SLC16A1	5	318	581	478	253	201	407	198	121	212	0.39	1.14E-02
P48509	CD151 antigen	CD151	1	108	143	343	66	81	57	67	81	80	0.38	1.10E-02
P49281-4	Natural resistance-associated macrophage protein 2	SLC11A2	2	362	494	558	271	149	135	236	79	147	0.33	3.47E-03
P04920	Anion exchange protein 2	SLC4A2	6	2459	2202	943	1538	469	933	674	575	526	0.32	2.78E-03
Q13467	Frizzled-5	FZD5	2	101	213	300	22	33	181	27	49	85	0.26	6.08E-04
Q96S97	Myeloid-associated differentiation marker	MYADM	1	94	87	75	29	58	43	18	14	26	0.23	1.65E-04
Q9H7M9	Platelet receptor Gi24	C10orf54	6	2365	2516	773	469	650	527	318	337	539	0.21	8.03E-05
Q9UIJ5	Palmitoyltransferase ZDHHC2	ZDHHC2	1	429	473	574	184	114	287	107	97	108	0.21	7.86E-05

P02724	Glycophorin-A (Unique)	GYPA Unique	128	64114	96792	86856	36597	35880	30445	19067	17062	11999	0.19	3.46E-05
Q8NBI5-2	Solute carrier family 43 member 3	SLC43A3	18	7025	7781	7281	1325	1652	1471	1317	1110	1331	0.17	8.49E-06
P14672	Solute carrier family 2, facilitated glucose transporter member 4	SLC2A4	4	1763	1931	1340	745	376	446	319	231	222	0.15	2.65E-06
O75387-2	Large neutral amino acids transporter small subunit 3	SLC43A1	11	3163	5231	3606	307	394	943	244	379	635	0.10	2.24E-08

List of all proteomic data from **Figures 2b**, **2c** and **Extended Data Figure 4.** n=3 biologically independent samples per genotype group. All 295 proteins either anchored in the RBC membrane or having a transmembrane region. Signal:noise values were normalised as described in the Methods. The method of significance A was used to estimate the p-value that each protein ratio was significantly different to 1, with adjustment for multiple testing using Benjamini-Hochberg correction. Colour coding in the table is matched to the coloured protein dots in the scatter plot in **Fig. 2b**, indicating significance p-value thresholds of fold change differences in protein expression between Dantu homozygote and non-Dantu RBCs: red - $p<0.0001$; green - $p<0.01$; light blue - $p<0.05$; dark blue - $p> 0.05$ (i.e. non-significant). Proteins are ordered by magnitude of fold change expression differences between Dantu homozygotes and non-Dantu. Note that Glycophorin-A is split into peptides unique to Glycophorin-A and peptides shared with Dantu.

Supplementary Table 5| Biomechanical properties of RBCs

	Non-Dantu (Mean ± SD)	Dantu heterozygote (Mean ± SD)	Dantu homozygote (Mean ± SD)
Number of samples	6	6	6
Number of cells	249	252	247
Bending modulus (10^{-20} J)	14.0 ± 1.5	14.0 ± 1.8	13.0 ± 2.7
Tension (10^{-7} N/m)	6.0 ± 1.9	7.9 ± 2.8	8.8 ± 0.7
Radius (μm)	4.2 ± 0.1	4.0 ± 0.1	3.9 ± 0.1
Viscosity (10^{-3} Pa s)	20.5 ± 5.6	20.8 ± 5.3	23.5± 4.6

The membrane mechanics of RBCs, measured with live video flickering spectrometry, were compared across Dantu genotypes. Six biological replicates were prepared for each genotype group. For each of these samples, the average RBC values for four mechanical parameters (bending modulus, tension, radius, and viscosity) were calculated from approximately 250 cells. The average values of the parameters from the six replicates were used to calculate the mean and SD for each genotype. Data shown in **Fig. 3a**.

Supplementary Table 6 | Impact of RBC tension on membrane deformation and parasite invasion

Invasion efficiency	**Genotype group**	**Number of cells**	**Tension (10^{-7} N/m)** (Mean ± SD)	**Deformation score**
Successful	non-Dantu	44	1.7 ± 1.2	2/3
	Dantu homozygotes	31	2.6 ± 2.2	2/3
Failed	non-Dantu	40	8.8 ± 5.7	0/1
	Dantu homozygotes	48	9.4 ± 4.9	0/1

The impact of tension on membrane deformation induced by parasites during pre-invasion, and on subsequent invasion, was compared across Dantu genotypes. Data shown in **Fig. 3c, d**.

Supplementary Table 7 | Glossary of Red Blood Cell Membrane Biophysical Properties

RBC biophysical properties	Unit of measurement	Definition	Techniques	Influence on *Pf* invasion
DEFORMABILITY (RIGIDITY/ STIFFNESS)	Deformability or elongation index	General term that describes the ability of a soft body to change its shape in response to an external force. Depending on the experimental protocol, it will correlate to a combination of RBC shape and size, cell viscosity, membrane bending and tension.	Ektacytometry, electric field, filtration (through microcontrictions).	Ligand binding to RBC increases its deformability [Sisquella 2017] Decrease in deformability reduces invasion in Malayan ovalocytes [Mohandas 1984]
Osmotic stress	Pa	Pressure due to imbalance of solutes across a semipermeable membrane. A sudden change in the solute concentration around a cell will cause a rapid movement of water across its cell membrane through osmosis – change in cell size, shape, hydration, viscosity, haemoglobin concentration, crowding. May correlate to a combination of RBC shape and size, cell viscosity, membrane bending and tension.	Osmometer for solution measurements. Assays of haemoglobin for intracellular crowding.	Dehydrated RBCs become denser and less susceptible to *Pf* invasion [Tiffert 2005].

VISCOSITY, η (dissipation in dynamical response. Note that in principle each of μ, E, κ, has a dynamical dissipative counterpart, but they have not been measured individually in RBC)	Pa s	Resistance to deformation at a given rate. As probed by various techniques, Viscosity combines membrane + cytoplasm viscosities. May correlate to a combination of RBC shape and size, membrane bending and tension.	Flickering, micropipette aspiration, AFM, parallel plate confinement, flow channels, filtration.	Higher viscosity in dehydrated (denser cells) correlates to reduced invasion [Tiffert 2005, Yoon 2009]
ELASTIC SHEAR MODULUS, μ	N/m^2 (or N/m for 2d)	A material property that describes the ability of a soft body to change its shape in response to an external force. It is well defined for a homogeneous material (3d block or 2d sheet) but in the context of a red blood cell it will correlate to a combination of RBC shape and size, membrane bending and tension.	Optical tweezers, micropipette aspiration, DPM	Decrease in deformability reduces invasion in Malayan ovalocytes [Mohandas 1984]
YOUNG'S MODULUS, E	N/m^2 (or N/m for 2d)	Given by stress/strain in a specific deformation geometry- Measures the resistance of a material to elastic deformations. It is proportional to the material property μ, for a given geometry of deformation.	AFM	

BENDING MODULUS, κ (or bending rigidity)	J	Energy required to bend a membrane, by changing its curvature. Depends on membrane asymmetry, thickness (including cytoskeleton and membrane proteins), lipid composition, lipid packing and order.	Flickering analysis, micropipette aspiration.	Decrease in membrane bending increases invasion efficiency [Koch 2017] **Our work:** Clearly decouples the effect of tension from any role for bending modulus
TENSION, σ (membrane extensional rigidity)	N/m	Force needed to stretch the membrane. Different regimes depending on the `excess surface area' of the cell membrane and on membrane-cytoskeleton adhesion. Once the membrane is taught, then depends on lipid composition.	Flickering analysis, micropipette aspiration, AFM, optical tweezers.	**Our work**: First link between increased tension and reduced invasion; later supported by theoretical modelling [Hillringhaus 2019]

Summary of techniques used to measure the biophysical properties of red blood cells in some exemplified publications [Tomaiuolo 2014, Kim 2015]. Individual cell analyses: flickering spectroscopy [Evans 2008, Yoon 2009, Koch 2017], diffraction phase microscopy (DPM) [Park 2008], pipette aspiration [Evans 1984], atomic force microscopy (AFM) [Dulinska 2006, Sinha 2015], and optical tweezers [Dao 2003, Popescu 2006, Yoon 2008, Sinha 2015].
Bulk cell analyses: ektacytometry [Mohandas 1984, Schrier 1989], filtration [Reid 1976], electric field [Engelhardt 1984], flow channels [Bow 2011].

1. Koch M, Wright KE, Otto O, et al. Plasmodium falciparum erythrocyte-binding antigen 175 triggers a biophysical change in the red blood cell that facilitates invasion. *Proc Natl Acad Sci U S A.* 2017;114(16):4225-4230.
2. Tiffert T, Lew VL, Ginsburg H, Krugliak M, Croisille L, Mohandas N. The hydration state of human red blood cells and their susceptibility to invasion by Plasmodium falciparum. *Blood.* 2005;105(12):4853-4860.
3. Sisquella X, Nebl T, Thompson JK, et al. Plasmodium falciparum ligand binding to erythrocytes induce alterations in deformability essential for invasion. *Elife.* 2017;6.
4. Tomaiuolo G. Biomechanical properties of red blood cells in health and disease towards microfluidics. Biomicrofluidics. 2014; 8(5):051501.

5. Kim J., Lee H., Shin S. Advances in the measurement of red blood cell deformability: A brief review. *J Cell Biothechnol*. 2015; 1(1):63-79.
6. Evans J, Gratzer W, Mohandas N et al. Fluctuations of the red blood cell membrane: relation to mechanical properties and lack of ATP dependence. *Biophys J*. 2008; 94(10): 4134-4144.
7. Yoon YZ, Hong H, Brown A, et al. Flickering analysis of erythrocyte mechanical properties: dependence on oxygenation level, cell shape, and hydration level. *Biophys J.* 2009;97(6):1606-1615.
8. Sinha A, Chu TT, Dao M, Chandramohanadas R. Single-cell evaluation of red blood cell bio-mechanical and nano-structural alterations upon chemically induced oxidative stress. *Sci Rep.* 2015; 5:9768.
9. Park Y, Diez-Silva M, Popescu G, *et al.* Refractive index maps and membrane dynamics of human red blood cells parasitized by Plasmodium falciparum *Proc Natl Acad Sci U S A*. 2008; 1051373013735.
10. Evans E., Mohandas N., Leung A. Static and dynamic rigidities of normal and sickle erythrocytes. Major influence of cell hemoglobin concentration*. J Clin Invest*. 1984. 73(2);477-488.
11. Dulinska I, Targosz M, Strojnv M et al. Stiffness of normal and pathological erythrocytes studied by means of atomic force microscopy. *J Biochem Bioph Meth*. 2006. 66(1-3):1-11.
12. Dao M, Lim C T and Suresh S. Mechanics of the human red blood cell deformed by optical tweezers. *J. Mech. Phys. Solids.* 2003. 51 2259.
13. Popescu G, Ikeda T, Goda K, et al. Optical measurement of cell membrane tension. *Phys Rev Lett.* 2006;97(21):218101.
14. Mohandas N, Lie-Injo LE, Friedman M, Mak JW. Rigid membranes of Malayan ovalocytes: a likely genetic barrier against malaria. *Blood.* 1984;63(6):1385-1392.
15. Schrier SL, Rachmilewitz E, Mohandas N. Cellular and membrane properties of alpha and beta thalassemic erythrocytes are different: implication for differences in clinical manifestations. *Blood.* 1989;74(6):2194-2202.
16. Reid H, Barnes A, Lock P et al. A simple method for measuring erythrocyte deformability. J. Clin. Pathol. 1976; 29855858.
17. Engelhardt H ,Gaub H, Sackmann E. Viscoelastic properties of erythrocyte membranes in high-frequency electric fields. *Nature.* 1984; 30 7378.
18. Bow H, Pivkin IV, Diez-Silva M et al. A microfabricated deformability-based flow cytometer with application to malaria. *Lab on a Chip*. 2011; 1110651073.
19. Hillringhaus S., Dasanna A. K., Gompper G., and Fedosov D. A. Importance of erythrocyte deformability for the alignment of malaria parasite upon invasion. *Biophys J*, 2019.

Supplementary Figure | Parasite preference invasion measured by flow cytometry

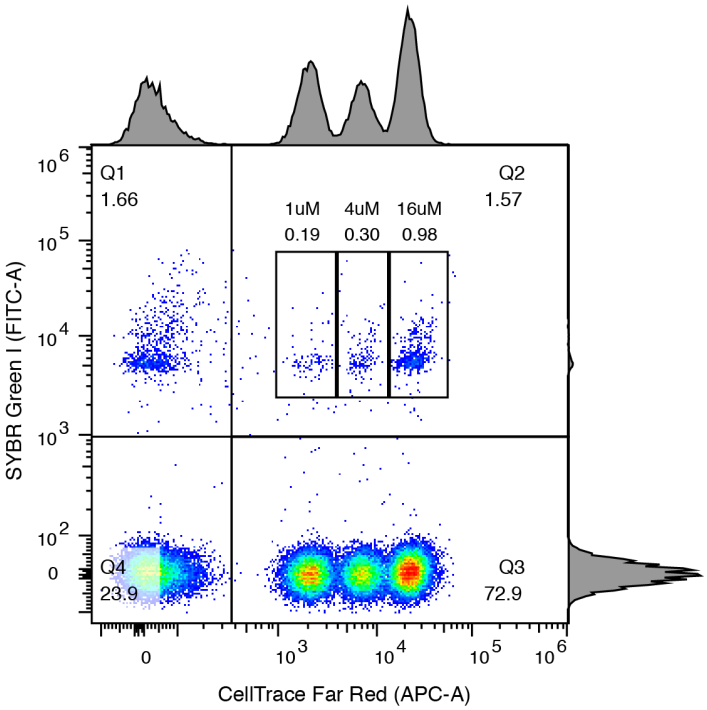

Parasite invasion preference for RBCs from donors across Dantu genotype groups (Dantu homozygous, Dantu heterozygous and non-Dantu) was measured using a flow cytometry-based preference invasion assay. RBCs from the three Dantu genotypes were differentially labelled with three concentrations of a fluorescent cytoplasmic dye, CellTrace Far Red (x-axis), distinguishing the three RBC populations, while parasite-infected RBCs were detected with a fluorescent DNA dye, SYBR Green I (y-axis). The dot plot represents preference invasion data from 3D7 laboratory parasite strain generated by flow cytometry, with the Dantu homozygous, heterozygous and non-Dantu RBCs labelled with 1uM, 4uM and 16uM CellTrace Far Red, respectively. The four distinguishable populations in the dot plot are: unlabeled, infected RBCs (upper left panel, “Q1”); labeled, infected RBCs (upper right panel, “Q2”); labeled, uninfected RBCs (lower right panel, “Q3”); and unlabeled, uninfected RBCs (lower left panel, “Q4”). Gates are drawn around the three clusters of labeled parasitised RBCs in Q2, with the percentage of parasitised RBCs in each cluster indicated. The flow-cytometry based preference invasion experiments were repeated three independent times with similar results.